REPORT DOCUMENTATION PAGE

Form Approved
OMB NO. 0704-0188

1. AGENCY USE ONLY (Leave Blank)	2. REPORT DATE December, 11th 2004	3. REPORT TYPE AND DATES COVERED Final Report 12-July-2000 - 11-September-2004

4. TITLE AND SUBTITLE
Spectral LADAR Receiver

5. FUNDING NUMBERS
DAAD19-00-1-0395

6. AUTHOR(S)
Brian A. Kinder and Dr. Eustace L. Dereniak

7. PERFORMING ORGANIZATION NAME(S) AND ADDRESS(ES)
The University of Arizona-Optical Sciences Center
1630 E. University Blvd.
Tucson, Arizona 85721

8. PERFORMING ORGANIZATION REPORT NUMBER

9. SPONSORING / MONITORING AGENCY NAME(S) AND ADDRESS(ES)

U. S. Army Research Office
P.O. Box 12211
Research Triangle Park, NC 27709-2211

10. SPONSORING / MONITORING AGENCY REPORT NUMBER

41485.4-PH

11. SUPPLEMENTARY NOTES

The views, opinions and/or findings contained in this report are those of the author(s) and should not be construed as an official Department of the Army position, policy or decision, unless so designated by other documentation.

12 a. DISTRIBUTION / AVAILABILITY STATEMENT

Approved for public release; distribution unlimited.

12 b. DISTRIBUTION CODE

13. ABSTRACT (Maximum 200 words)

The Ranging Imaging Spectrometer (RIS) combines hyperspectral and LADAR imaging capabilities in a single system, allowing both ranging and spectral discrimination to be performed. The RIS couples the Scannerless Range Imaging LADAR developed at Sandia National Laboratories with a Computed Tomographic Imaging Spectrometer (CTIS) operating between 600 nm and 900 nm to provide a hyperspectral snapshot-based imaging and ranging spectrometer. The output of the system is four-dimensional, (x, y, z, and λ) data cube.

The RIS spectral resolution is 10 nm; it has been demonstrated to 19nm. Its angular resolution is 2.8 mr; and its range resolution is 17.5 cm. It collects spectral samples in a 77 x 77 pixel format with angular subtend of 12.5°. The laser emitter wavelength is 857 nm.

This report documents the RIS design, construction, testing, and range and spectral calibrations. It details solutions to the problems encountered in coupling the two systems, including (optimizing the CTIS for the 857-nm wavelength) and development of a range correction technique that reduces error in range reconstruction by a factor of 10.

14. SUBJECT TERMS	15. NUMBER OF PAGES
none	67
	16. PRICE CODE

17. SECURITY CLASSIFICATION OR REPORT	18. SECURITY CLASSIFICATION ON THIS PAGE	19. SECURITY CLASSIFICATION OF ABSTRACT	20. LIMITATION OF ABSTRACT
UNCLASSIFIED	**UNCLASSIFIED**	**UNCLASSIFIED**	**UL**

Table of Contents

List of Appendixes, Illustrations and Tables

Statement of the problem studied

The goal of this project was to develop an instrument that is able to simultaneously measure 3-D spatial and hyperspectral information. The instrument hinges on the fact that the Computed Tomographic Imaging Spectrometer (CTIS) produces a set of contiguous spectral images in the wavelength range of interest from one integrated frame (snapshot). The CTIS is able to obtain the spectral data by spatially encoding the information on a commercially available 2-D focal plane using a custom Computer Generated Holographic Disperser (CGH).

Originally, it was proposed to add a pulsed laser system to an existing CTIS and extract phase information about the reflected laser pulse from the spectral image containing the laser wavelength. However, Sandia National Labs developed a technology called the Scannerless Range Imaging LADAR (SRI LADAR) that uses a heterodyning technique to measure time-of-light using a series of rapidly acquired images using a commercially available CCD camera (which is very similar to the originally proposed concept).

It was decided to borrow a SRI LADAR from Sandia that operated at 857nm and develop and integrate a CTIS instrument. The CTIS can be attached to the front of the LADAR replacing the existing objective lens. The LADAR itself is quasi-monochromatic because it contains a narrowband optical filter centered on the laser wavelength. This filter is placed in the receiving optics and prevents ambient light from entering the system and affecting the range measurement. In order to integrate the two systems, this filter had to be removed to make the instrument broadband over the spectral region of interest. The combined instrument called the Ranging-Imaging Spectrometer (RIS) would then be capable of simultaneously measuring 3-D and hyperspectral data (x, y, z, and λ) from 600nm – 900nm in a series of snapshots using a single focal plane array. The problems faced in developing the instrument were:

- Bore-sighting the two systems without vignetting either field of view.
- Optical Design of the CTIS from 600nm – 900nm around LADAR operating wavelength.
- By removing the optical filter, the LADAR range accuracy diminished due to the increased ambient light.

- Effect of the CTIS optics on lateral resolution.
- Effect of the high intensity laser light on spectral resolution.

Abstract

The Ranging Imaging Spectrometer (RIS) combines hyperspectral and LADAR imaging capabilities in a single system, allowing both ranging and spectral discrimination to be performed. The RIS couples the Scannerless Range Imaging LADAR developed at Sandia National Laboratories with a Computed Tomographic Imaging Spectrometer (CTIS) operating between 600 nm and 900 nm to provide a hyperspectral snapshot-based imaging and ranging spectrometer. The output of the system is four-dimensional, (x, y, z, and λ) data cube.

The RIS spectral resolution is 10 nm; it has been demonstrated to 19nm. Its angular resolution is 2.8 mr; and its range resolution is 17.5 cm. It collects spectral samples in a 77 x 77 pixel format with angular subtend of 12.5^{o}. The laser emitter wavelength is 857 nm.

This report documents the RIS design, construction, testing, and range and spectral calibrations. It details solutions to the problems encountered in coupling the two systems, including (optimizing the CTIS for the 857-nm wavelength) and development of a range correction technique that reduces error in range reconstruction by a factor of 10.

Introduction

A variety of information can be optically gathered from a scene including spatial information from cameras, spectral information from spectrometers, and range information from laser detection and ranging (LADAR) instruments. This information can be used to find certain minerals in mining operations, to navigate autonomous vehicles, or to perform military reconnaissance. In these applications, there is a need to rapidly acquire the data in order to capture dynamic events. There is also a need to combine the spectral and ranging capabilities into a single instrument. A new instrument has been developed called the Ranging-Imaging Spectrometer (RIS). This RIS combines current techniques in imaging spectrometry and range imaging for use on a single focal plane array (FPA) and acquires the data with multiple images.

The design and analysis of the instrument is presented. Spectral and range calibration techniques and analysis of the systems performance are detailed. A novel technique for range error correction using random variable statistics was developed and is also presented.

System Concept

The instrument is a combination of two well-established technologies, the Computed Tomographic Imaging Spectrometer (CTIS) and the Scannerless Range Imaging LADAR (SRI LADAR). The resulting system simultaneously captures range and spectral information on a single focal plane array (FPA).

The CTIS uses a Computer Generated Holographic (CGH) disperser to diffract passive light from the scene. The light is then imaged onto a FPA and it is then read into a computer where the spatial and spectral data can be reconstructed using mathematics similar to that of limited angle tomography. The spectral images are reconstructed using either Multiplicative Algebraic Reconstruction Technique (MART) or Expectation Maximization (EM) or a combination of both. The SRI LADAR uses phase encoding to measure the Time of Flight (TOF) for each pixel. The phase information is encoded by heterodyning outgoing laser pulses with a modulated receiver gain. Range of the scene is calculated on a per pixel basis using a TOF algorithm using a sequence of images with differing amounts of phase between the laser pulses and gain modulation.

These two instruments can be bore sighted for use with a single FPA to produce an instrument capable of simultaneously measuring spectral and three dimensional (3-D) spatial data. This data can be represented as a four dimensional hypercube with one spectral (λ) dimensions and three spatial (x, y, and z) dimensions. This data is referred to as the spatial-spectral hypercube; a conceptualization is shown in figure 1.

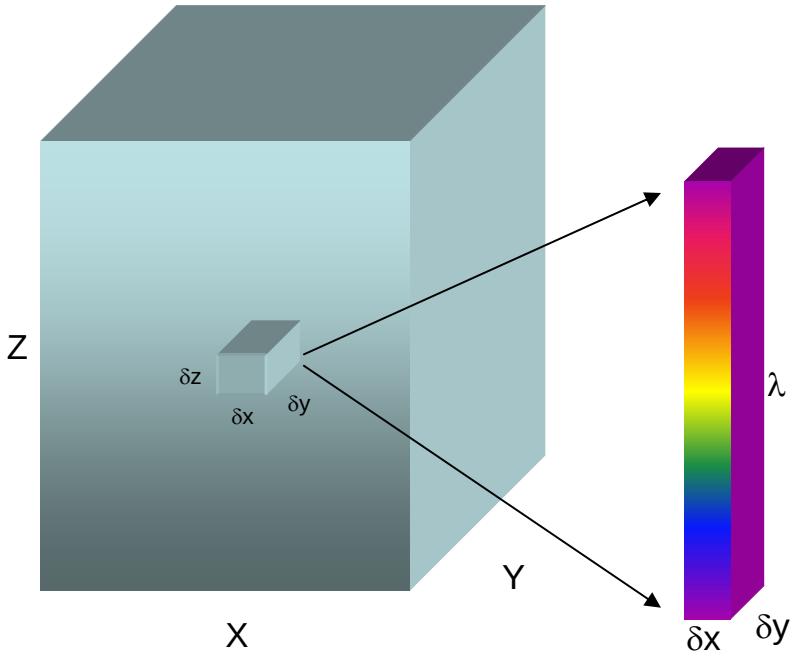

Figure 1: Conceptualization of the four-dimensional spatial-spectral data hypercube.

Subsystem Descriptions:

Computed Tomographic Imaging Spectrometer (CTIS)

The goal of any imaging spectrometer is to collect spectral data for each pixel in the image. The data contained in the scene can be interpreted as a construct called the object cube. The object cube is the continuous 3-D representation of the spatial and spectral information contained in a scene. Instruments, due to the finite size of their resolution elements, are unable to capture continuous information. Instead they compartmentalize the data into a set of voxels that make up the best "estimate" of the object cube called the data cube. Figure 2 illustrates the voxel representation of the continuous object cube. The dimensions of the voxels and data cube are determined by their spatial and spectral sample sizes and the field of view and spectral passband of the instrument respectively.

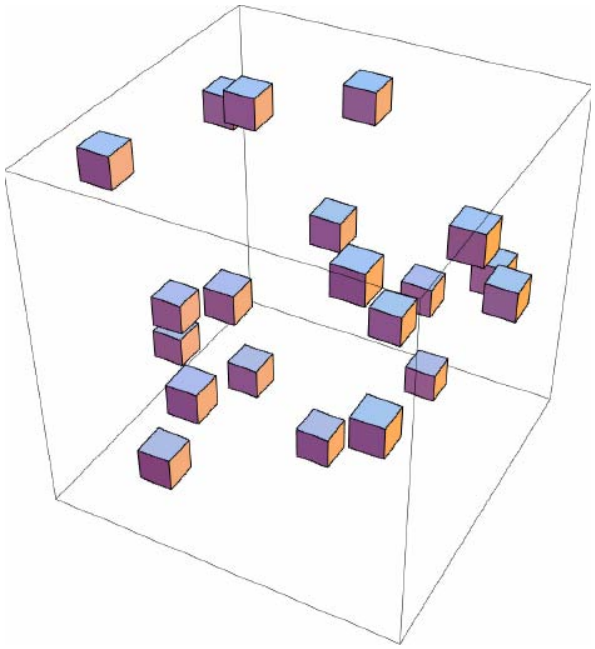

Figure 2: Illustration of the voxelated object cube.

The Computed Tomographic Imaging Spectrometer (CTIS) is capable of measuring the spectral data cube in a single integration time on a 2-D focal plane. Instead of scanning across one dimension of the object cube, it uses diffractive optics to project the object cube onto the focal plane. CTIS is primarily composed of off-the-shelf optical components and contains no moving parts. Figure 3 is a diagram of the optical layout of the CTIS.

The CTIS images the scene onto a field stop located at the front focal point of a second lens called the collimator. The collimated light then passes through a Computer Generated Holographic (CGH) disperser. The diffraction pattern is then imaged onto the focal plane.

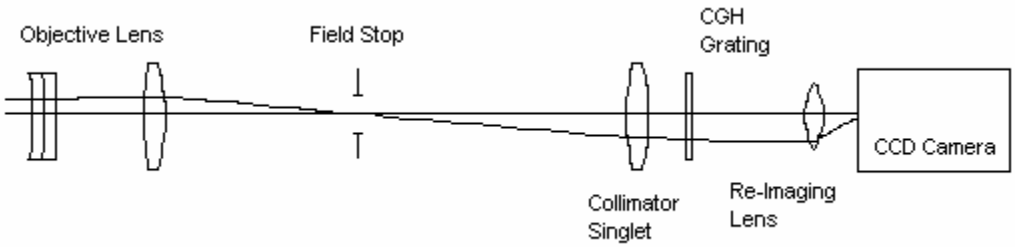

Figure 3: Diagram of the optical layout of the CTIS

The CGH diffraction grating is the workhorse of the system. It produces a diffraction pattern similar to that of two crossed linear gratings; however the efficiency of the CGH grating has been tailored to contain the light in the lower diffraction orders. The center, or 0^{th} diffraction order, is a panchromatic image of the scene. The spatial extent of the 0^{th} order on the array defines the spatial sampling of the system. The higher diffraction orders are the image of the scene are smeared out spectrally. The spectral spread increases with diffraction order, defining the spectral resolution. It is this "smearing" of the image that allows the CTIS to measure the spectral content of the scene.

Each individual diffraction order is a projection of the object cube onto a 2-D surface. Figure 4 is an illustration of the object cube projection.

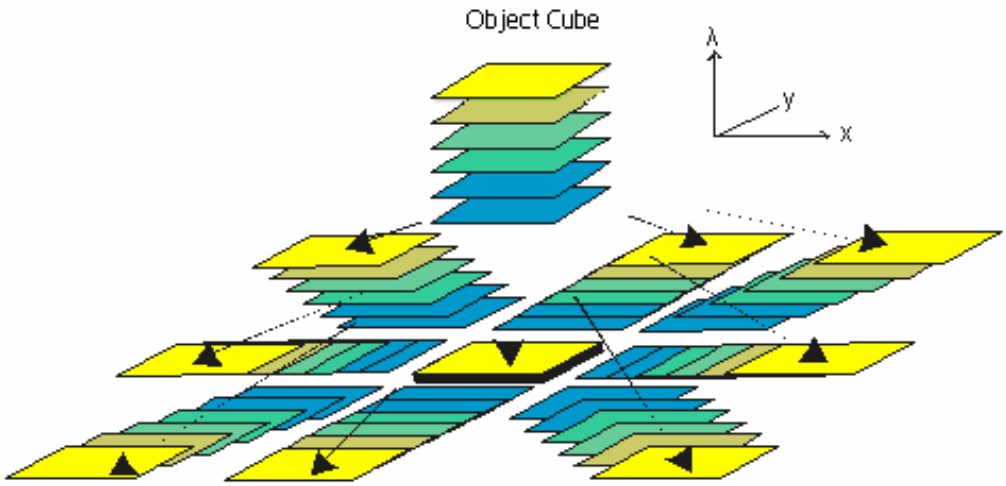

Figure 4: Illustration of the Object cube projections.

The diffraction order number determines the projection angle through the object cube. This projection technique is analogous to limited-angle tomography. An estimate of the object cube is then reconstructed from these projections using tomographic reconstruction techniques (Expectation Maximization or Multiplicative Algebraic Reconstruction Technique).

It is directly apparent from the projection model that the size of the focal plane array and the pixel size determine both spectral and spatial resolution. The extent of the focal plane only allows a limited number of diffraction orders to be captured, permitting only a finite sampling of the object cube. For this reason, there is a tradeoff existing between spectral and spatial resolution. The spatial resolution is limited by the size of the field stop. The larger the field stop, the greater the spatial sampling but a fewer number of diffraction orders can fit on the FPA. Conversely, a small field stop has low spatial sampling but allows more diffraction orders can fit on the FPA. Since we are also using diffractive optics, the spectral extent of the object cube is restricted to one octave before the orders begin to overlap. All issues listed above are taken into consideration in the optical design of the CTIS components.

Scannerless Range Imaging LADAR (SRI LADAR)

The Scannerless Range Imaging Laser Ranging And Detection (LADAR) was developed at Sandia National Labs in Albuquerque, NM. An image of the system is contained in Figure 5. The LADAR uses a Time of Flight (TOF) algorithm to determine the range to the scene. Unlike other instruments, this LADAR captures data without spatial scanning across the field of view. Mechanical architecture of this type is ideal for working with the CTIS instrument.

The instrument is based on a Kodak 10-bit camera with 1532 x 1024 pixels. The camera has been outfitted with a laser emitter and a gated image intensifier. The laser emitter, located on the top of the camera, consists of two piggybacked laser diodes with wavelengths of 857nm. The output of the diodes, modulated at 1kHZ, is expanded into a 2” diameter beam by a cylindrical lens. The beam then passes through a holographic diffuser. The holographic diffuser confines radiation to 80% of the laser to a cone angle of 40° while making the system eye safe. The objective lens images the scene onto the cathode of a gated image intensifier. The generated electrons pass through a micro channel plate (MCP) where they are multiplied before they strike the phosphor screen. A voltage is applied to the MCP to control the amount of applied gain. The gain has a DC offset and is sinusoidally modulated at 10MHz. The MCP is also gated to allow laser

return from the desired range interval and to limit ambient light. The output of the phosphor screen is transferred to the focal plane of the camera via fiber optic taper.

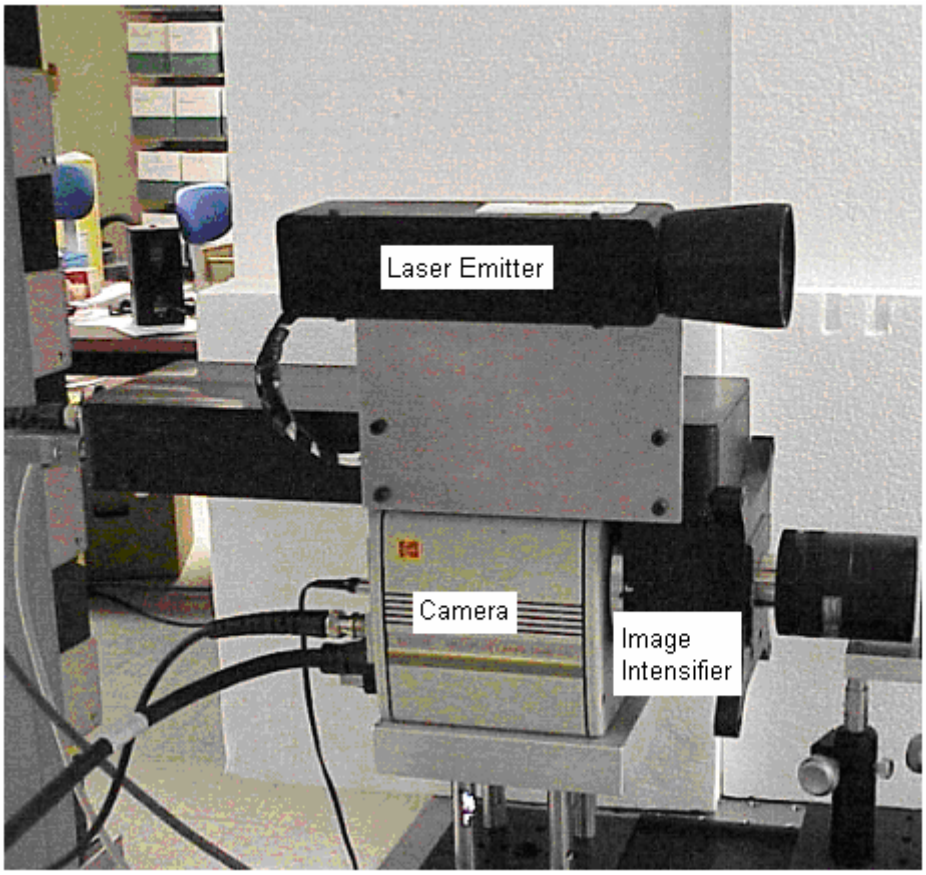

Figure 5: Image of the SRI LADAR.

The image intensifier and the laser emitter in combination are responsible for determining range. The two waveforms, the laser pulses and the MCP gain are heterodyned, and the resulting image intensity is range dependent.

Time of Flight Algorithm Description

The LADAR uses a Time of Flight algorithm injunction with heterodyning to measure range. Time of Flight refers to the amount of time that it takes for light emitted from the laser source to reflect off of an object and be imaged onto the FPA. Since light travels at the fixed speed c, the distance D to the target is given by:

$$D = c/2t \qquad [1]$$

Therefore the farther a target is away from the instrument, the greater the Time of Flight.

The technique developed by Sandia, called the Scannerless Range Imaging (SRI) technique, floodlight illuminates the scene with diffuse laser light. The average intensity of the reflected laser light that has been heterodyned with the modulated gain from the image intensifier is then recorded by a conventional FPA. Sequences of intensity images, called phase images, are obtained at discrete steps of 45° in the relative phase difference between the emitter and receiver waveforms. The algorithm determines range using a relationship between intensity and phase or frequency of modulation. The advantages to this technique are that no spatial scanning is required and it can be used with conventional focal plane technology. An in-depth description of the technique, as contained in Smithpeter et. Al. [2], is contained in the following paragraphs.

The signal produced by the laser emitter is pulsed at a rate of 1000Hz and the gain signal is sinusoidally modulated at 10MHz. The receiver (RCV) and transmitter (XMT) waveforms are periodic; they can be represented by Fourier series (2 and 3).

$$XMT(t) = A_0 + \sum_{i=1}^{\infty} A_i Cos(i2\pi f_0 t + \alpha_i) \quad [2]$$

$$RCV(t) = B_0 + \sum_{j=1}^{\infty} BjCos(j2\pi f_0 t + \beta j + j\theta_n) \quad [3]$$

The fundamental frequency is given by f_0 and the relative phase difference between the receiver and transmitter is given by θ_n, where n is the image number. The indices i and j refer to the harmonic order of the waveform and α_i and the β_j are fixed components of the transmitter and receiver at each harmonic respectively. The light that illuminates a target at range R and at times, t is due the light that was emitted at (t-R/c) and will be imaged at (t+R/c). The instantaneous pixel brightness of the nth image (I_n(t+R/c)) can be expressed as:

$$I_n(t + R/c) = [A_0 + \sum_{i=1}^{\infty} A_i Cos(i2\pi f_0 (t - R/c) + \alpha_i] * [B_0 + \sum_{j=1}^{\infty} B_j Cos[j2\pi (t + R/c) + \beta_j + j\theta_n] \quad [4]$$

Here the coefficients A and B contain both sensor and scene dependent parameters. These parameters include reflectance and ambient light levels.

In this system, the fundamental frequency (f_0) is 10Mhz. Since the time constant of the phosphor screen in the intensifier and the integration period of the camera

(nominally 250ms) are over many periods of the fundamental frequency, the DC component of the signal is detected. Since all time dependant terms are sinusoidal they average to zero over the integration time, equation 4 simplifies to equation 5.

$$I_n = A_0 B_0 + \frac{1}{2}\sum_{i=1}^{\infty} A_i B_i Cos\{\frac{4\pi f_0 iR}{c} + \beta_i - \alpha_i + i\theta_n) \quad [5]$$

Here the subscript i denotes the harmonic order of the waveform relative to the fundamental frequency. For A_i and B_i to be non-zero it is necessary for the harmonic to be present in both waveforms. Since the gain modulation contains only the fundamental frequency, equation 5 contains only three unknowns, A_0B_0, A_1B_1, and R. Because there are only three unknowns, a minimum of three images are needed to determine range. To generalize the algorithm, we assume that R is constant over the series of N images and that the phase increments are equal such that:

$$\theta_n = 2\pi n / N \quad [6]$$

The discrete Fourier transform may be applied to $I_{n,}$ for i = 1 to (n-1)/2 yielding:

$$\{\frac{A_i B_i}{2} Cos(\frac{4\pi f_0 iR}{c} + \beta_i - \alpha_i)\} \cong \frac{2}{N}\sum_{n=1}^{N} I_n Cos(\frac{2\pi ni}{N}) \quad [7]$$

$$\{\frac{A_i B_i}{2} Sin(\frac{4\pi f_0 iR}{c} + \beta_i - \alpha_i)\} \cong -\frac{2}{N}\sum_{n=1}^{N} I_n Sin(\frac{2\pi ni}{N}) \quad [8]$$

From this, one can state that:

$$\{\frac{4\pi f_0 R}{c} + \beta_1 - \alpha_1\} \cong ATAN(\frac{-\sum_{n=1}^{N} I_n Cos(\frac{2\pi ni}{N})}{\sum_{n=1}^{N} I_n Sin(\frac{2\pi ni}{N})}) \quad [9]$$

The resulting equation is the Time of Flight algorithm. It is efficient having a full 2π relative range interval that is independent of any initial estimate of the A and B coefficients. The left hand side of equation 9 is called the relative range term. The β_1-α_1 is a constant associated with the timing delay in the electronics. This term is calibrated for each of the range intervals, and the calibration procedure is reserved for a later section.

The particular instrument used for the RIS uses a sequence of eight images (N = 8). Therefore the phase step between each successive image in the sequence is $\pi/4$. Once

the sequence of images is captured, the software developed by Sandia calculates the range on a per pixel basis using the following expanded version of Equation 9.

$$\frac{4\pi f_0 R}{c} + \beta_1 - \alpha_1 \cong ATAN\left[\frac{\frac{-\sqrt{2}}{2} I_1 - I_2 - \frac{\sqrt{2}}{2} I_3 + \frac{\sqrt{2}}{2} I_5 + I_6 + \frac{\sqrt{2}}{2} I_7}{\frac{\sqrt{2}}{2} I_1 - \frac{\sqrt{2}}{2} I_3 - I_4 - \frac{\sqrt{2}}{2} I_5 + \frac{\sqrt{2}}{2} I_7 + I_8}\right] \quad [10]$$

The LADAR is limited to a relative range bin of 15m due to the 10MHz modulation frequency of the receiver. It is capable of measuring over several range bins provided there is an adequate laser return.

At this point it is necessary to introduce some nomenclature used to describe the images captured by the instrument. The sequence of eight images that are taken by the LADAR to be used for the range construction are raw data and are hereafter referred to as "phase images" or "phase frames". Once the range has been calculated using the phase images, the data are processed and the resulting image is hereafter referred to as a "range image" or "range frame". An example of a series of phase images of a Styrofoam target and the calculated range image are shown in figures 6 and 7 respectively.

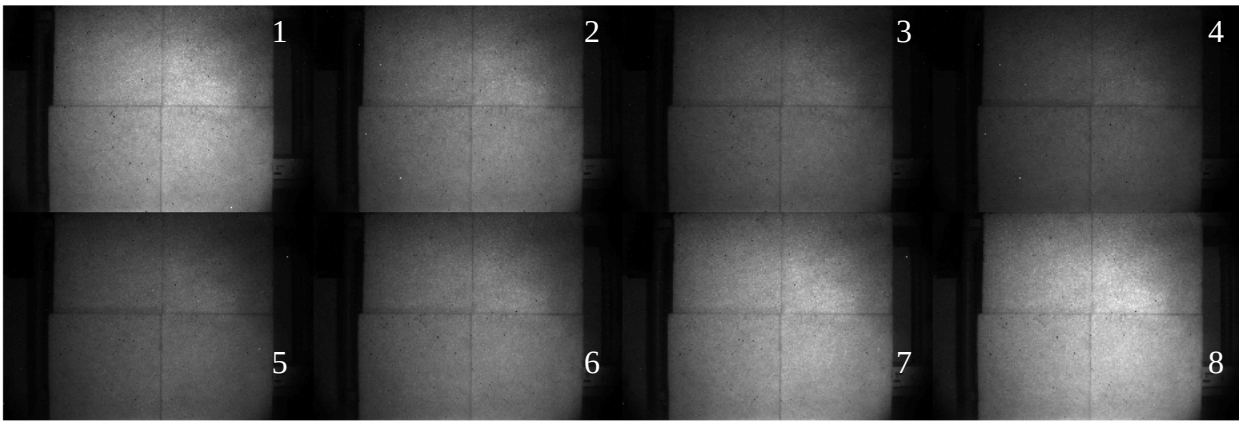

Figure 6: Phase image sequence of a Styrofoam target. The number in the upper right of each of the sub-images denotes its order taken.

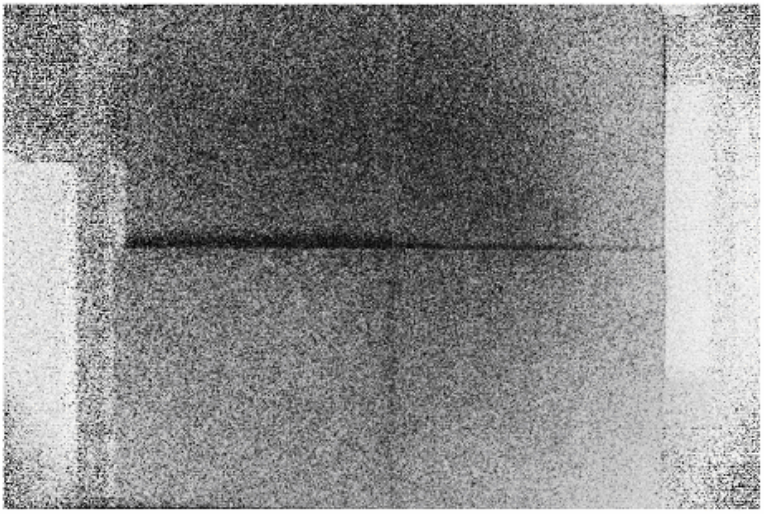

Figure 7: Range image reconstruction for the phase image sequence from Figure 6.

Work completed

CTIS Optical Design: The system is based on an existing LADAR system operating at 857nm. The CTIS had to be designed to fit the specifications of the existing LADAR. The CTIS is attached to the front of the LADAR receiver replacing the existing objective lens. A diagram of the RIS is shown in Figure 8.

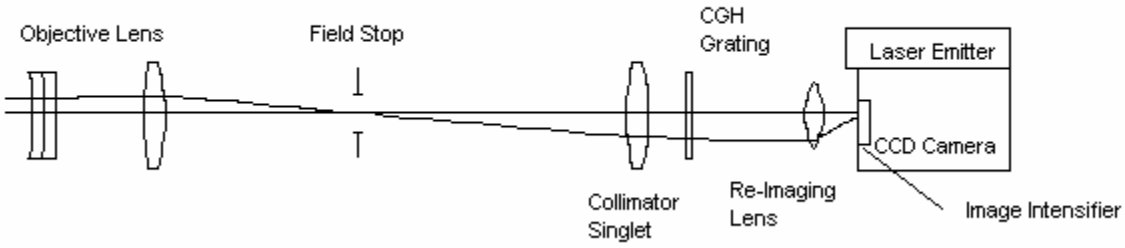

Figure 8: Diagram of the RIS.

As stated previously, the CTIS was designed around a current LADAR system, built by Sandia National Labs. Arrangements were made to have the system loaned for this project. Their system uses two 857nm laser diodes that are pulsed at a rate of 1 kHz that serve as the laser emitter. The laser beams are shaped using a cylindrical lens to fill the aperture of a holographic diffuser. The holographic diffuser spreads the emitted laser radiation to floodlight illuminate the target. The diffuser confines 80% of the laser

energy into a projected full field of 20°. The light is then reflected off of the target and collected by the CTIS. The CTIS images then the scene on the intensifier of the LADAR. The image intensifier is a standard scientific grade manufactured by ITT (FS9910 Series) that has a gated microchannel plate (MCP). The output of the phosphor screen of the image intensifier relayed to a CCD camera via a fiber optic taper. The camera is a Kodak MegaPlus 1.6i 10-bit camera.

Since the LADAR operates in the near infrared (NIR), the lenses used in the CTIS need to be corrected for aberrations in that wavelength region. A line of off-the-shelf CCD camera lenses by Schneider Optics corrected in the NIR and low dispersion glass singlets by Janos were used in the optical design.

In order for the entire scene viewed by the imaging optics to contain range information, the diffuser projection angle must be greater than the field of view of the receiving optics. A geometrical calculation was performed to determine the field of view of the receiver. Based on the fieldstop size and available NIR corrected lenses, a lens from Schneider Optics called Xenoplan was chosen for the CTIS objective lens. The CTIS objective lens has a focal length of 22.5 mm, yielding a full field of view of 12.732°.

The CTIS optical design is also highly dependent on the spectral region where the instrument will operate, and the dimensions of the focal plane array. Since the LADAR operates at 857nm and uses a 1024 x 1532 pixel array with a pitch of 9μm, the CTIS passband has to include that wavelength, and the collimating and re-imaging optics need to be chosen such that the image will fit on the array. The LADAR also uses a fiber optic taper to transfer the image from the phosphor screen of the intensifier to the FPA. Any magnification induced by the taper must also be considered.

First, a wavelength band from 600 – 900 nm was chosen due to: the off-the-shelf NIR corrected optics that was available at that time, the etch depth required to build the CGH grating, and the response of the image intensifier and CCD array. Next, the maximum size of the image on the image intensifier must be determined. To determine the maximum image size, the magnification induced by the fiber taper must be measured.

The taper magnification measurement was carried out by placing a grid of known spacing on the faceplate of the intensifier. Images were taken and the number of pixels

across the grid was counted and the size was compared to the actual grid, resulting in the magnification factor of 1.015. The dimensions of the focal plane are then divided by this number to yield an effective image size on the intensifier. Lastly, the collimating and re-imaging lens of the CTIS (fig. 8) are then determined using a geometrical design approach [1]. The optical components that were determined using this program are as follows:

Field Stop	5mm square	Vendor
Collimator Lens	Plano-convex, efl = 500 mm	Janos (A0704-715)
Re-Imaging lens	C-mount, efl = 70.2 mm	Schneider (Tele-Xenar)

Table 1: CTIS components list determined using the design code

The fieldstop and the two lenses are off-the-shelf components. The collimator lens is made of Barium Fluoride (BaF_2) from Janos, which has a very small change in the index of refraction over our wavelength interval. The re-imaging lens is a standard C-mount lens manufactured by Schneider Optics and is corrected for the NIR. Below, in figure 9, is a computer simulation of the image that is formed on the cathode of the image intensifier of the LADAR system by the CTIS.

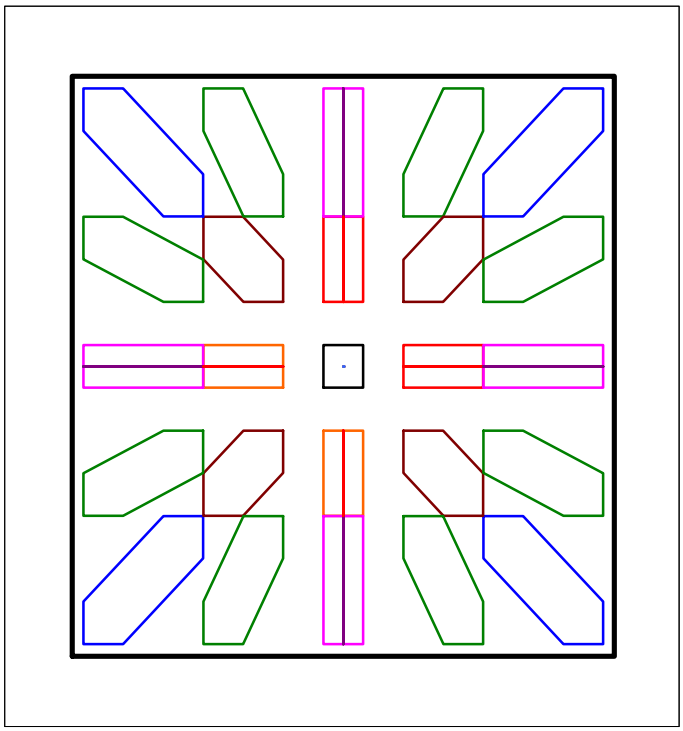

Figure 9: FPA Image Model

The CTIS diffraction grating was designed to use ± 2 diffraction orders for the reconstruction. The use of any higher orders would give greater spectral resolution, sacrificing spatial resolution. The center order is approximately 75 x 75 pixels square. Also, in this design there is no overlap of the diffraction orders. This makes the reconstruction of the object easier eliminating crosstalk between wavelengths [5].

Computer Generated Holographic Disperser:

A Computer Generated Holographic (CGH) disperser was fabricated by JPL. The disperser was designed by Chris Tebow using a grating design program written by Curtis Volin (both formerly of the Optical Detection Lab). The disperser is designed to uniformly distribute the energy across the desired orders from 600-900 nm.

The CGH disperser used in the Ranging-Imaging Spectrometer is a phase grating that is composed of an 8 x 8 pattern that is tiled over the entire area of the grating. The tiled pattern is composed up of 4 micron square pixels that are electron beam etched to the calculated depths, giving the corresponding phase delay determined by the grating design program. The pattern is 19 mm in diameter on a 25.4 mm diameter substrate. A profile of the grating was obtained using a WYKO interferometer. The profile is used qualitatively verify that the grating was fabricated correctly. Figure 10 below is a portion of the grating viewed by the interferometer showing the relative pixel heights.

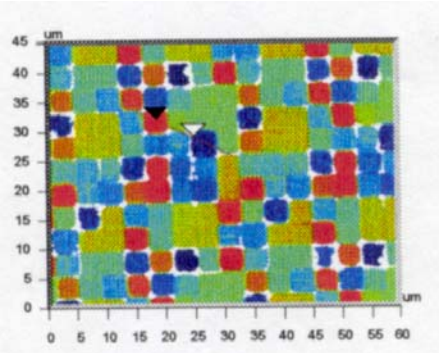

Figure 10-a: Small portion of the CGH. Red areas are peaks and blue are valleys.

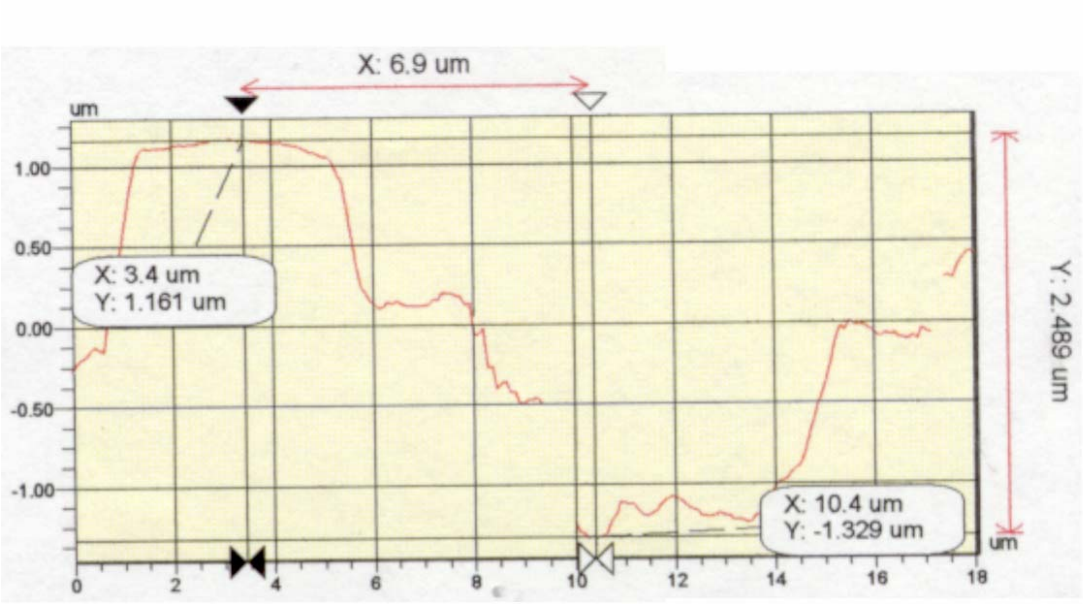

Figure 10-b: Shows a depth change in adjacent pixels on the CGH. (Note that the widths of the pixels, is approximately 4 microns as designed.)

Opto-Mechanical Design of the CTIS:

For ease and simplicity, off-the-shelf components were used as much as possible. There were two major design considerations for the system: 1) Have components that can be rotated and x-z adjustable and 2) to be able to mate the CTIS to an existing LADAR system.

The instrument needed to have the ability to rotate the fieldstop and the grating so that the final image is aligned both vertically and horizontally with the pixels on the focal plane. The rotation issue for the field stop was solved by designing a custom mount that has a rotating shaft. This was done by fabricating an outer cylinder that has the objective lens mounted to it. Then a rotating inner cylinder is inserted into the outer cylinder. The fieldstop is mounted in the inner cylinder at the appropriate distance away from the objective lens. This allows the scene to be focused in the field stop but allows for rotation to align the edges of the fieldstop with the pixels. The rotating inner piece is then held in place with three setscrews. A diagram of the objective mount is shown in figure 11. The rotation of the CGH grating was addressed by mounting it in an off-the-shelf polarizer mount, which can be rotated and locked in position with a set screw.

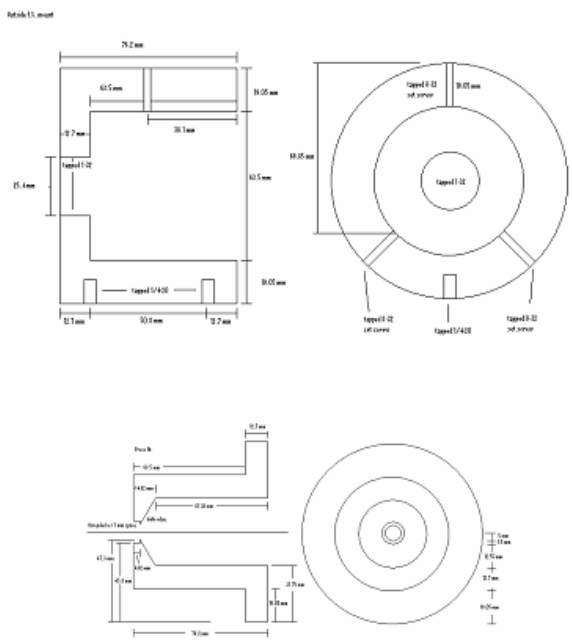

Figure 11: Diagram of the objective mount.

It is also advantageous to have the distance between the grating and the collimating lens, and the distance between the collimating lens and re-imaging lens to be as short as possible to prevent vignetting. The proximity issue between the grating the collimating lens was solved by mounting the singlet lens holder for the collimator directly to the polarizer mount. This mounting technique has a gap of only a few millimeters between the two elements. The two elements were then attached to a custom bar that, when placed on two optical posts, prevents skew rotation.

Each of the component mounts are placed on adjustable height posts making them adjustable in vertical (x) direction. The posts are attached to an optical rail with sliders that allow for adjustment in the z direction (along optical axis). No adjustments are needed in the horizontal (y) direction because the optical axes of elements are confined in the x-z plane by the posts and sliders.

The final step was to light proof the system. An aluminum tube was cut to length and mounted in a groove cut into the objective mount. A notch was cut in it so it can slide over the grating/collimator assembly.

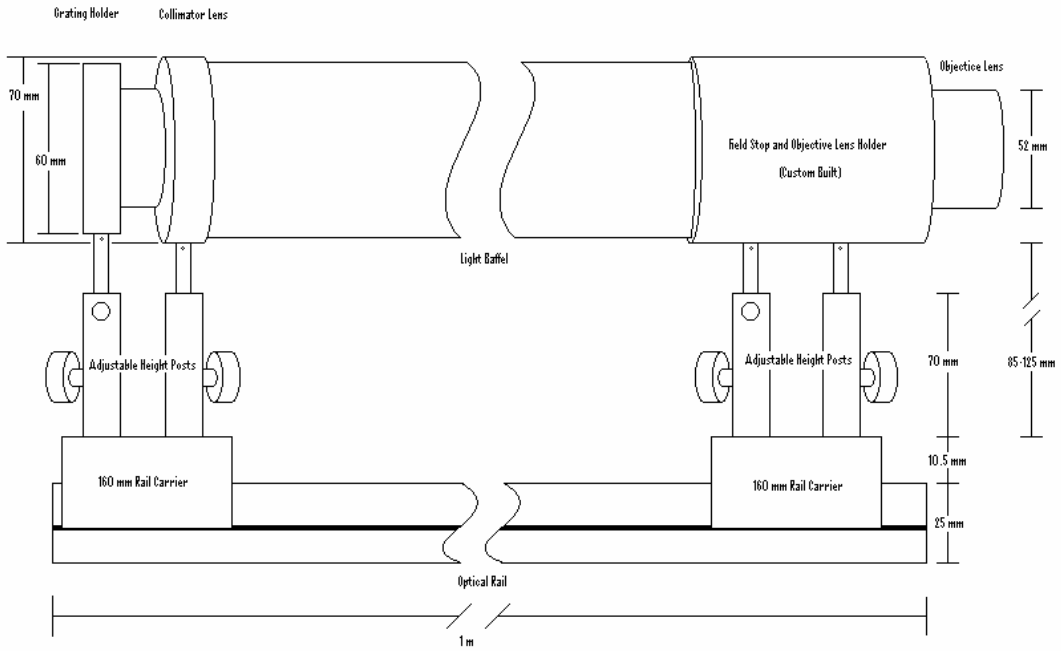

Figure 12-a: Diagram of CTIS subsystem

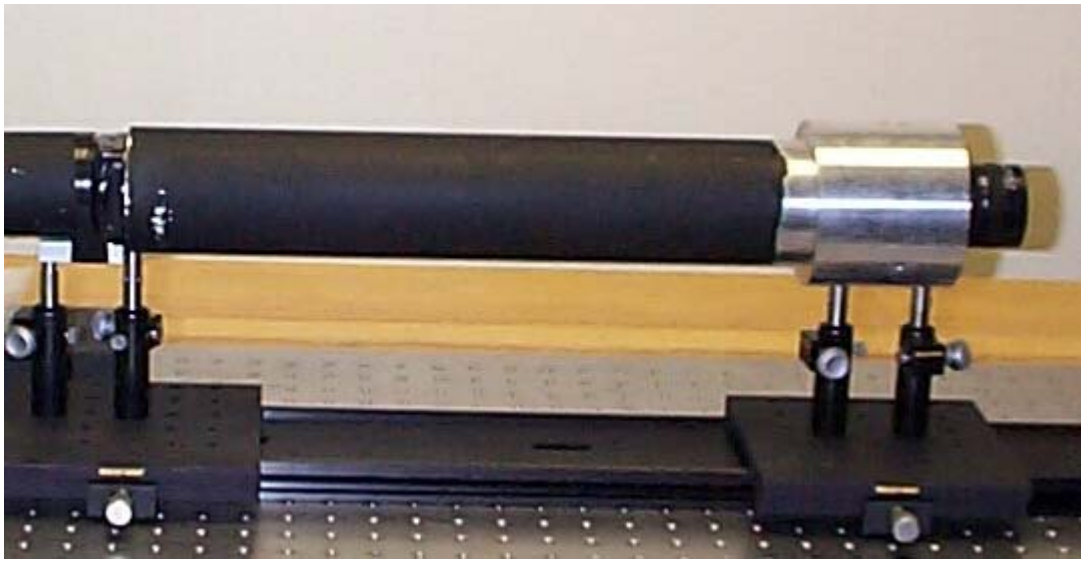

Figure 12-b: Image of the CTIS subsystem.

Opto-mechanical Design of the LADAR Mount:

The LADAR was built on the chassis of a standard Kodak CCD camera. To combine the two systems, a custom mount for the camera was made. It allowed the camera to be kinematically mounted to an optical breadboard. The thickness of the mount was such that it corresponded to the middle of the range of the adjustable height

posts on the CTIS. The optical rail for the CTIS was butted up to the base of the kinematic mount of the LADAR and the two were bolted to an optical breadboard. The re-imaging lens could be screwed in to the LADAR using the existing standard c-mount, and the height of the CTIS was adjusted using the posts such the optical axes of the two systems were aligned. A second aluminum pipe was used as a light baffle between the re-imaging lens on the LADAR and the collimator lens on the CTIS. Images of the LADAR and the mount are shown in figure 13.

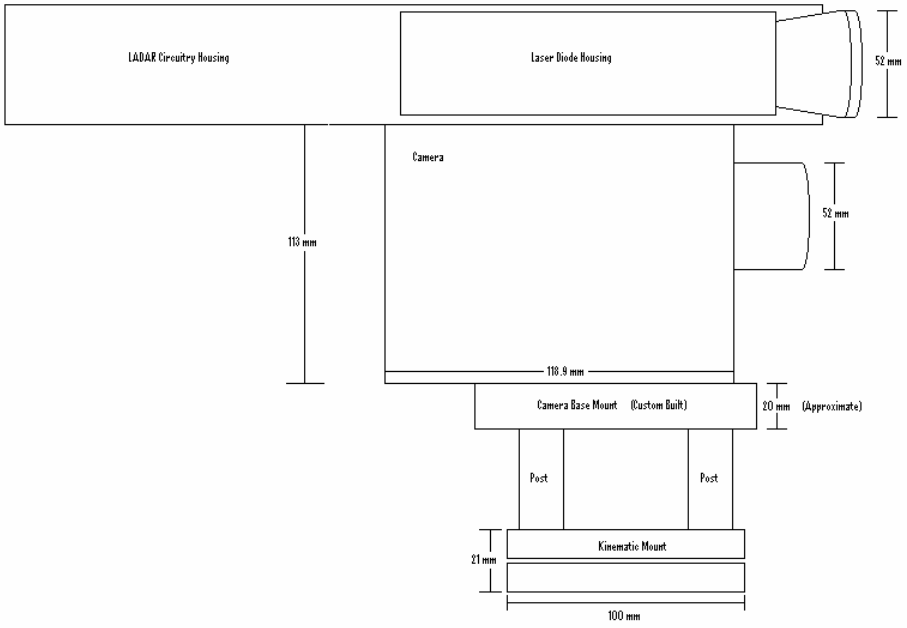

Figure 13-a: Diagram of the mounted LADAR system.

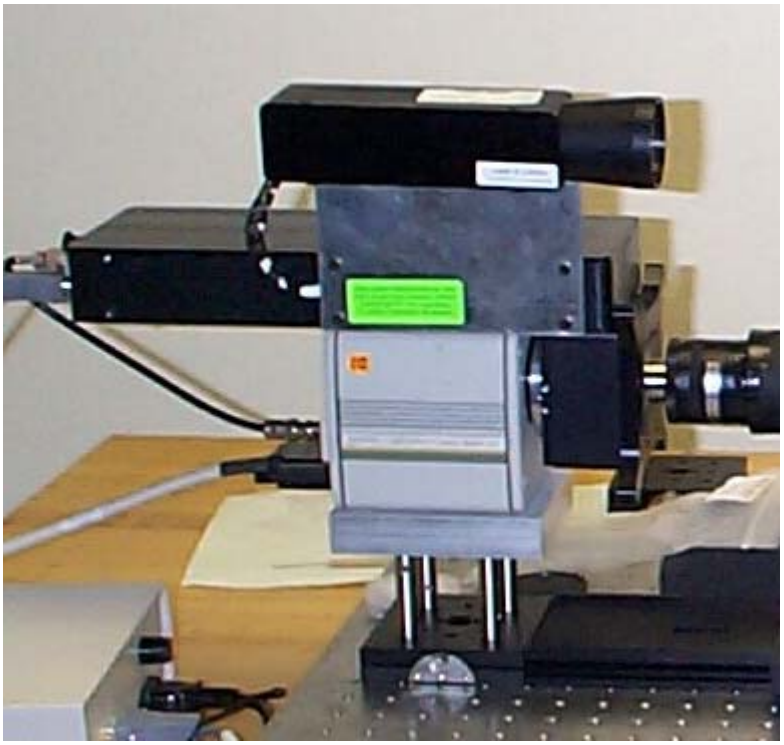

Figure 13-b: Image of the mounted LADAR system

Height Adjustment of the Laser Emitter:

One other integration issue that came up in the system design comes from the diffusing angle of the laser beam that is emitted from the LADAR. The holographic diffuser has a full field angle of 40° and was mounted as close to the optical axis of the receiving optics as possible. With the CTIS attached to the front of the LADAR, the objective lens is about 80cm in front of the laser emitter. When the laser would fire, a portion of the diverging beam would be blocked by the CTIS casting a shadow on the scene. With the laser light blocked, no range information can be recovered from the portion of scene contained in the shadow.

A simulation in IDL was performed to model the shadow cast by the CTIS. The distance between the two optical axes was increased until the shadow was out of the field-of-view of the CTIS. The result of the simulation was to raise the height of the laser illuminator by 4 in. Below in figure 14 are two images produces by the program showing the shadowing effect.

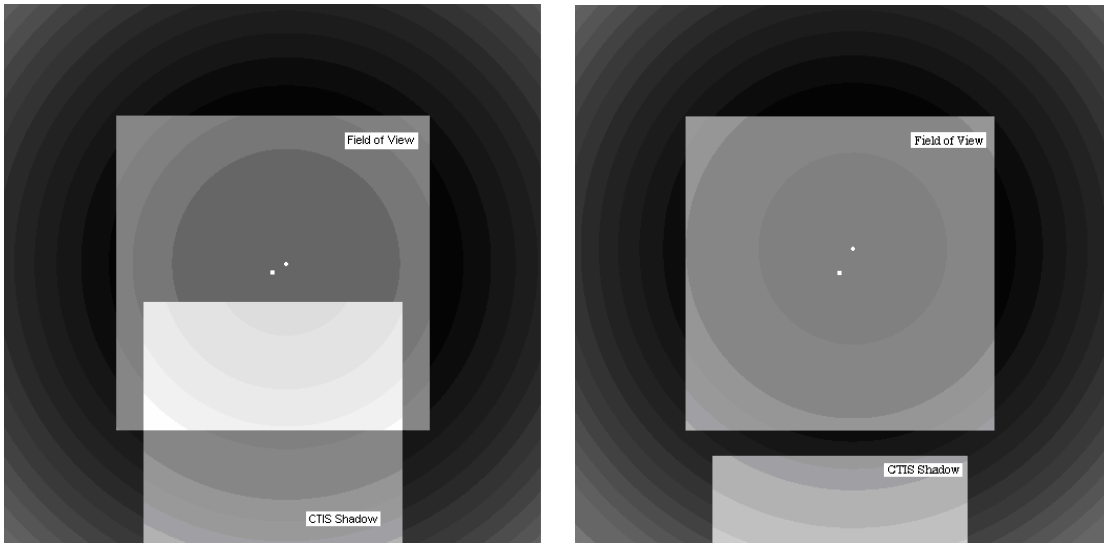

Figure 14: In the above images the centered square is the field of view of the CTIS and the center of the field is marked with a small white square. The center of the laser illumination is marked with a small circle. The lower square represents the shadow cast by the CTIS. The image on the left shows that the laser illumination is blocked by the CTIS, showing that the height needed top be corrected. The image on the right shows the shadow produced has been moved out of the field of view.

RIS Assembly:

With the height of the laser emitter adjusted, the CTIS and LADAR were brought together, and the instrument is assembled. Below in figure 15 is an image of the Ranging-Imaging Spectrometer.

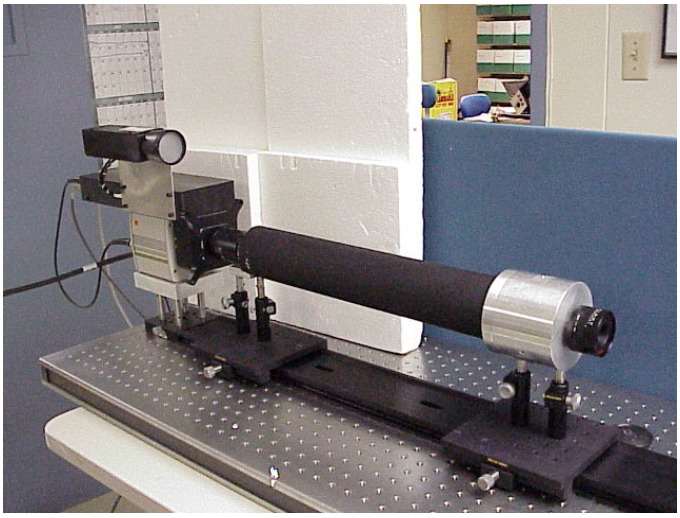

Figure 15: Image of the Ranging-Imaging Spectrometer.

With the RIS assembled, data was taken. However, since the LADAR had not been cleared to leave Sandia at this point, the system was not calibrated. Despite that fact, images were taken to show the system was working as intended. Images of a flat Styrofoam target were acquired with and without ambient illumination. The target was placed 2m in front of the RIS and was large enough to fill the field of view. The room lights were turned off and the target was illuminated with a photographer's lamp to provide ambient illumination. Images were acquired with and without the illumination from the photographer's lamp.

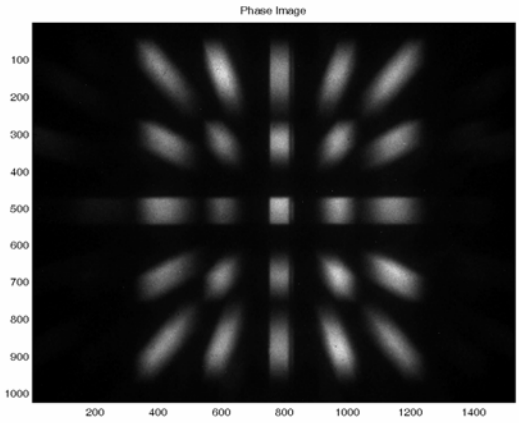

Figure 16: RIS image with high background illumination and with the laser blocked showing the 5 x 5 diffraction pattern as designed by the grating. Note the similarities between the actual data and the simulated image in figure 9.

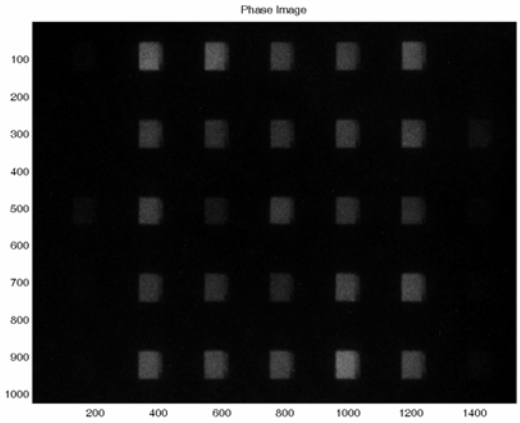

Figure 17: Image showing a full field target illuminated with the 857nm laser emitter of the RIS. (Note: When compared to Figure 16, the spectral image corresponding to the laser line falls off near the outside edge of the diffraction orders.)

Spectral Calibration:

The LADAR was finally cleared to leave Sandia and was shipped to The University of Arizona where it was reassembled. The completed system was then calibrated spectrally. The spectral calibration of the RIS (spectral calibration setup is shown in figure 18) is performed in the same manner as in a conventional CTIS and is explained in the following paragraphs.

The system is assumed to be shift-invariant and is governed by the continuous-to-discrete imaging equation

$$\mathbf{g} = \mathbf{H} * \mathbf{f} + \mathbf{n}, \qquad [11]$$

where **f** is a continuous object, **H** is the system matrix of the RIS, **n** is noise, and **g** is the discretized image. One can get an estimate of **f**, called **f-hat**, by multiplying **g** by the pseudo inverse of **H**, called $\mathbf{H}^{+}$ [Eq. 12]**.**

$$\mathbf{f\text{-}hat} = \mathbf{g} * \mathbf{H}^{+} \qquad [12]$$

An estimate of **f** can only be calculated due to the finite limit on spatial sampling and inherent noise of the system.

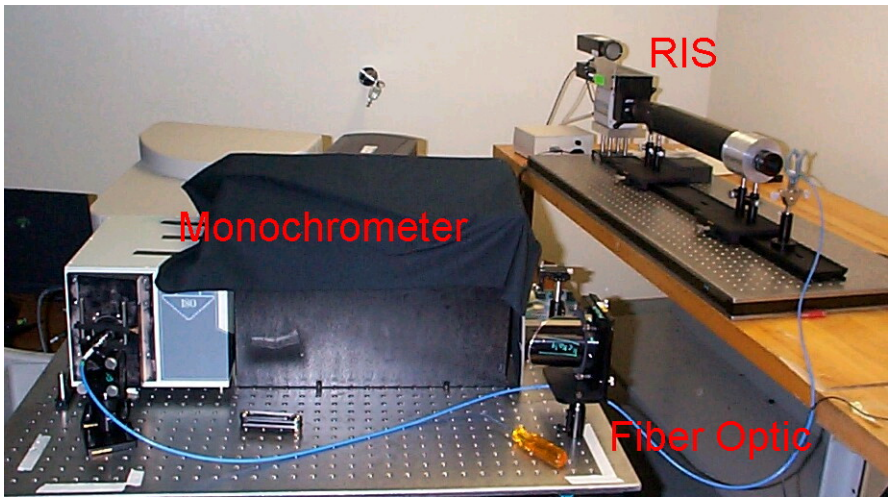

Figure 18: Image of the spectral calibration setup

H is found by taking a series of images though the system at different wavelengths. For example, in the absence of noise **n** and if the object **f** in equation 11 is unit one (1), the image **g** is then equal to the matrix **H**.

It should be noted the during the spectral calibration procedure, the output from the laser emitter was blocked to only allow the signal on the detector be generated from the monochromator light. Also, since the signal from the monochromator is continuous and the integration time of the camera occurs over a large number of image intensifier modulation periods, there is no intensity modulation across the 8 phase images.

To create a unit one input for our system, a monochromator is used to generate a narrow band (5nm – 10nm) source at each wavelength of interest for the calibration. The output of the monochromator is coupled into an optical fiber. The output facet of the fiber is then imaged onto the fieldstop of the RIS by the objective lens. The image in the fieldstop is then relayed to the focal plane through the rest of the optical train of the RIS generating a point spread function (PSF). With the PSF known, the system matrix **H** can be determined [8].

In order to determine **H** in its entirety, a PSF must be measured at each wavelength of interest for every pixel in the fieldstop. Performing this calibration would be exhaustive; therefore a hybrid approach is taken. To perform the spectral calibration, a PSF measurement is taken at each wavelength of interest, but only for one pixel in the fieldstop. Using the shift-invariant assumption, the PSF is then shifted around to each pixel in the fieldstop by the computer and an **H** matrix is constructed. To ensure the best measurement of the PSF, the image of the fiber is adjusted such that the center order of the diffraction pattern covers the fewest number of pixels. Ideally, the center order image should cover only one pixel, but due to dispersion in the optics the image was 3 to 5 pixels across depending on the wavelength.

To generate the system matrix, several images are taken at each wavelength of interest and averaged. Then dark frames are taken, averaged, and subtracted to improve the signal to noise ratio. The images are scaled to remove any signature from the calibration source (Reference detector responsivity (η_{ref}) and reference measurement value (I_{ref}), and to account for the integration time of the camera (T_{int}). The processed image is referred to as a spectral intensity point spread function and the mathematics are shown in equation 13.

$$\textbf{S-IPSF} = (\textbf{Image} * \eta_{ref}) / (I_{ref} * T_{int}) \quad [13]$$

The RIS was calibrated spectrally three different times. The first spectral calibration was carried out from 600nm – 900nm with $\Delta\lambda$ = 10nm providing 31 spectral samples. For this calibration, 240 images were taken with the monochromator on and 48 dark images were taken at each wavelength. This first spectral calibration was also carried out using a 100W bulb in the monochromator. Due to the low responsivity of the image intensifier at the long wavelengths in the band, the images acquired from 870nm – 900nm were unusable. A processed image from the first calibration at 600nm is shown in figure 10.

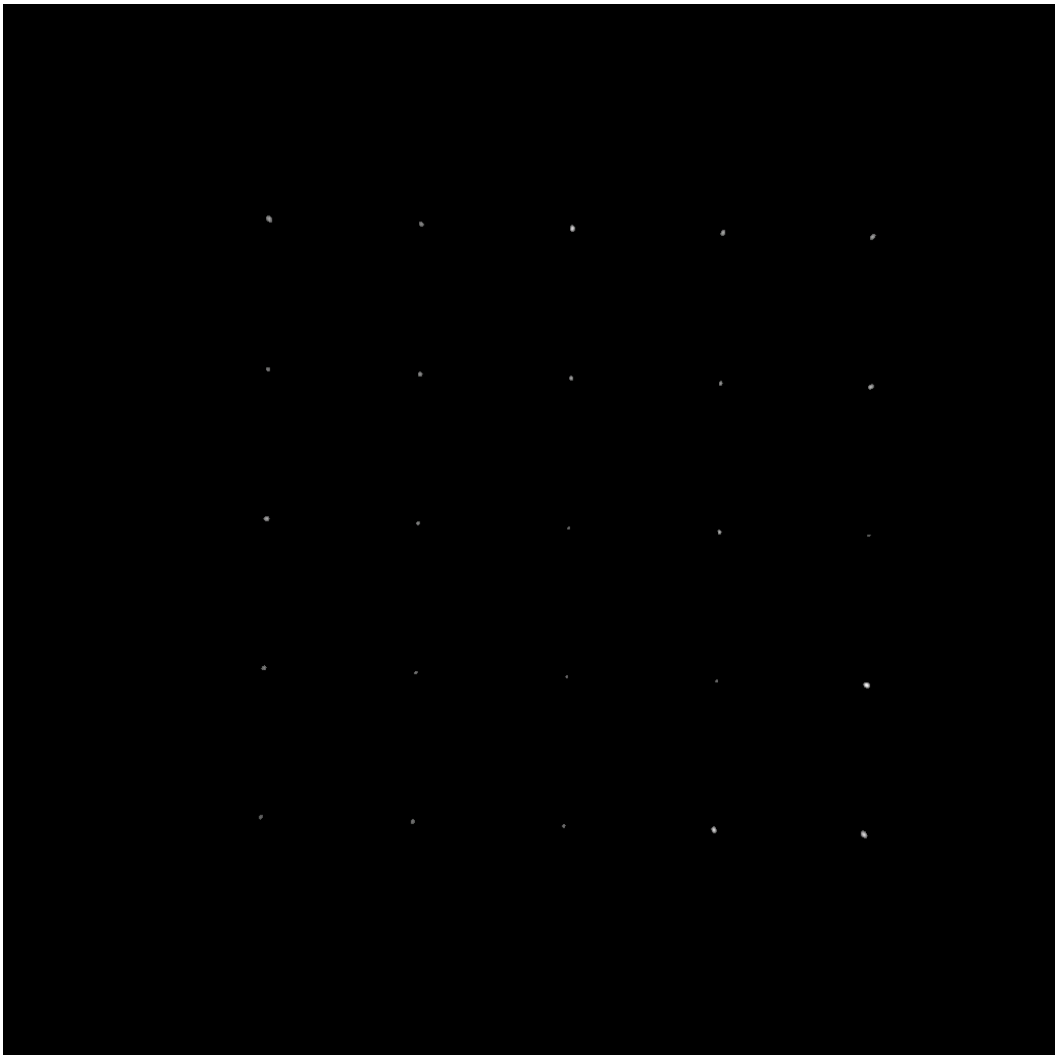

Figure 19: Spectral Intensity Point Spread Function of the RIS at 600 nm. The image shows the 5 x 5 order diffraction pattern produced by the CTIS.

The second spectral calibration was performed using a 100W bulb in the monochromator but the images were shifted to shorter wavelengths by 3nm. This shift in the calibration wavelengths was carried out in order to have a spectral sample that is closer to the laser wavelength. The third and final spectral calibration was carried out for system using a 250W bulb the monochromator. The higher wattage bulb improved the signal to noise ratio for the calibration images near the long wavelength end of the spectrum because it emitted more light. The final calibration of the system was from 597nm-897nm in 5 nm steps yielding 61 spectral samples. Please note that throughout the remainder of the document; spectral images are reconstructed using the different spectral calibrations previously mentioned. The calibration wavelengths are noted either in the figure captions or in section headings.

Spectral Calibration Confirmation:

To verify the spectral calibration and the software, test objects were imaged with the RIS and reconstructed. The reconstruction is performed with two iterative algorithms, called Expectation Maximization (EM) and Multiplicative Algebraic Reconstruction Technique (MART). These algorithms can be used individually or in combination. They use the 0^{th} order projection of the CTIS diffraction pattern as the first estimate of **f** and converge to a solution.

The spectral calibration was confirmed by performing the reconstruction using two of the images used to calibrate the system. The two calibration images were superimposed in the computer and then inputted into the reconstruction program using the two algorithms mentioned above. The test image consists of a single point that contains light at 600 nm and 750 nm only [Fig. 20].

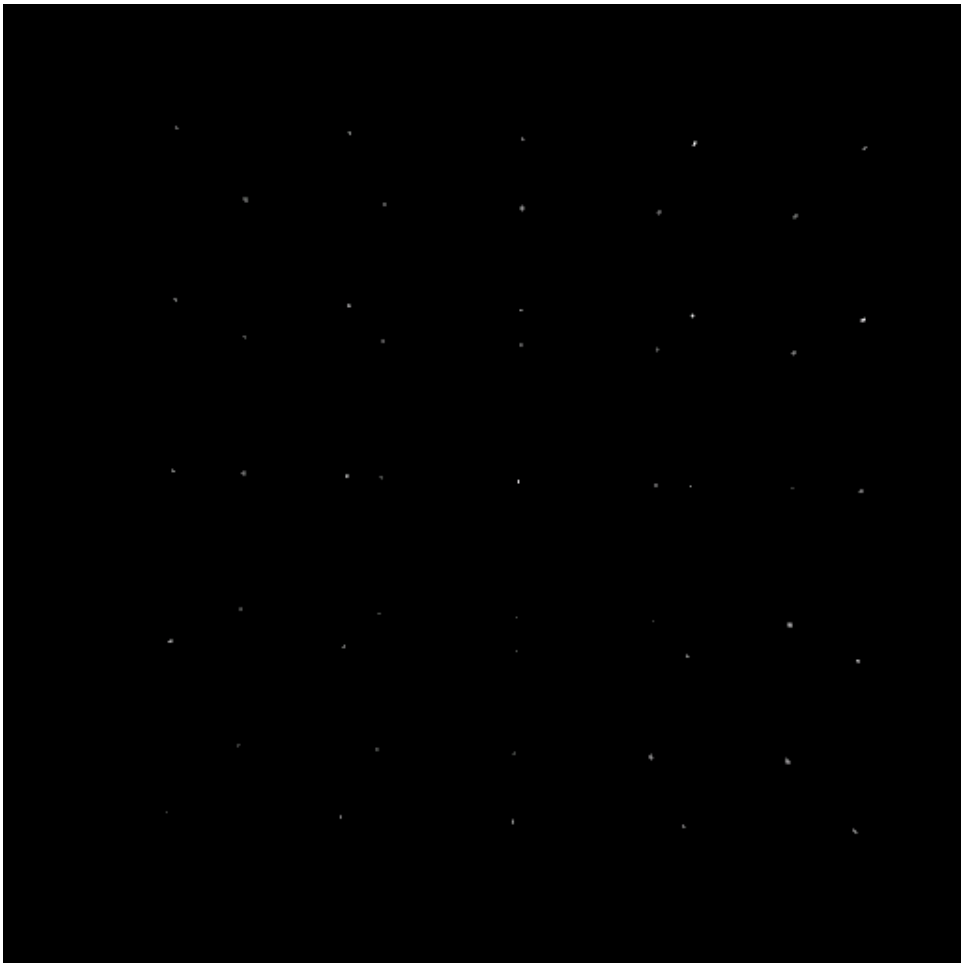

Figure 20: Simulated image formed from two S-IPSF's, 600 nm and 750 nm

The image was reconstructed using 5 iterations of the Mart and 5 iterations of the EM algorithms. Below [Fig. 21] is the reconstructed normalized relative spectrum of the point-like object (Note the two peaks at 600 nm and 750 nm). There is a small peak at 900 nm due to poor quality calibration images at 890 nm and 900 nm.

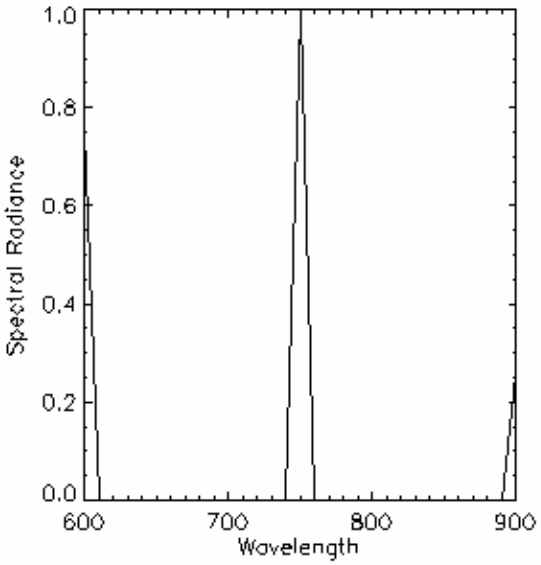

Figure 21: Reconstructed spectrum, from 600nm - 900nm with $\Delta\lambda$ = 10nm, of the simulated object consisting of 600 nm and 750 nm wavelengths.

Next the two wavelengths were separated spatially by shifting the 750 nm image 10 pixels to the right of its original position in the computer. The new object was then reconstructed and the spectrum was obtained for the two points [Fig. 22].

The reconstruction of the object in figure 22 shows that the individual spectrums taken at each point produce the two different spectrums. The two spectrums peak at the appropriate places corresponding to their wavelengths.

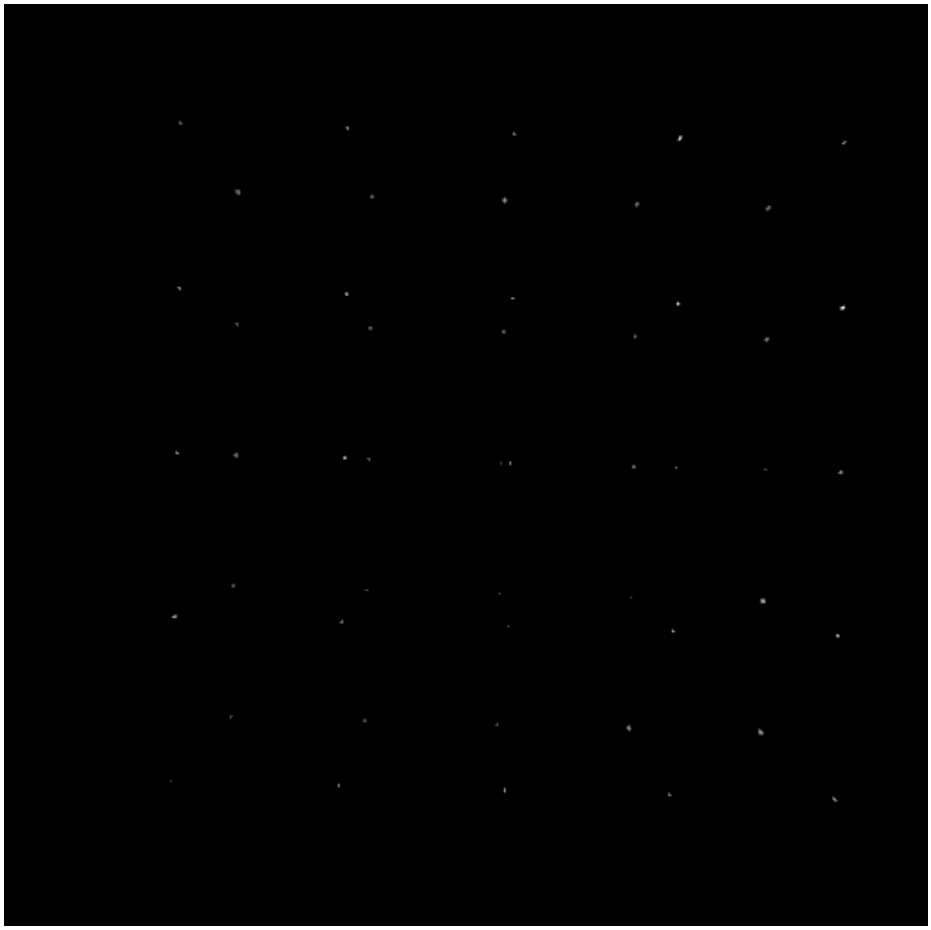

Figure 22: Simulated object with the 750 nm point shifted 10 pixels to the right of the 600 nm point.

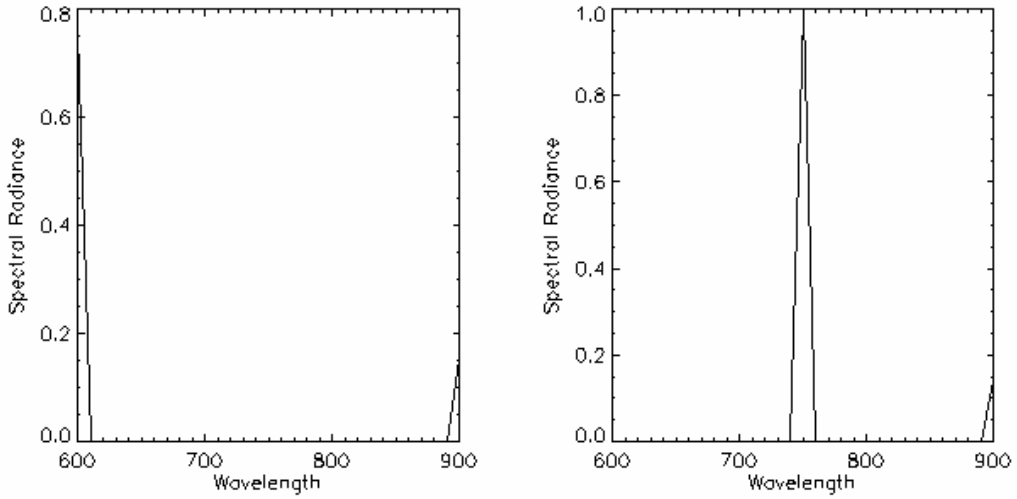

Figure 23: Reconstructed spectrums of the shifted simulated object consisting of 600 nm and 750 nm light using the 600nm - 900nm with $\Delta\lambda$ = 10nm calibration.

The system was next tested on a physical object. The physical test object was a white ceramic coffee cup illuminated with tungsten and fluorescent light bulbs, and a laser pointer with a wavelength of 647 nm [Fig. 24]. During this test, the laser emitter at 857nm was blocked. The image captured of the coffee cup test by the RIS is shown in Figure 25.

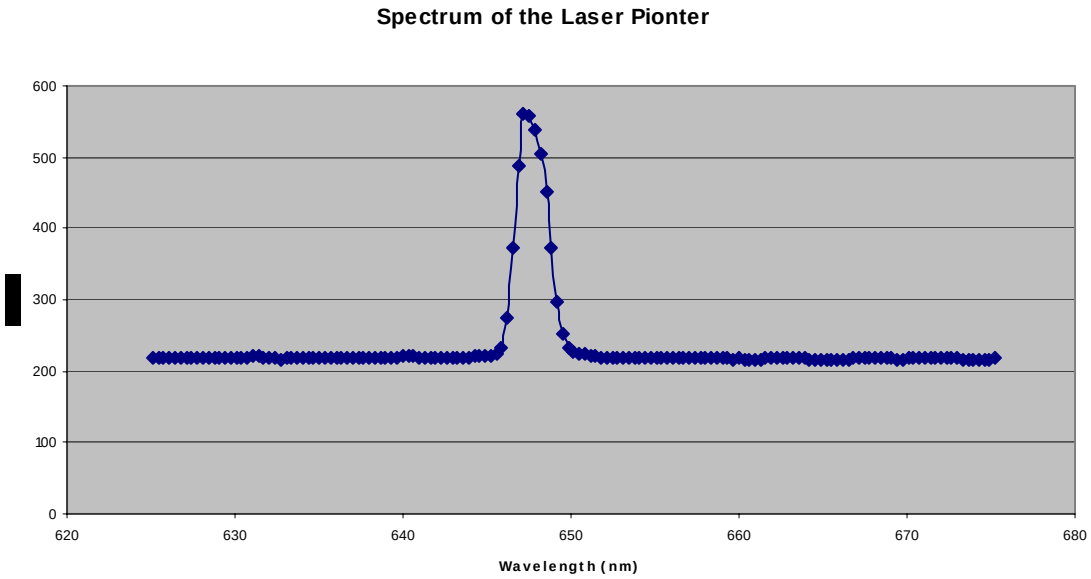

Figure 24: Spectral measurement of the laser pointer showing a peak wavelength of 647 nm using an Ocean Optics spectrometer.

The spectrum was reconstructed using 5 iterations of MART and 5 iterations of EM [Fig. 26]. Images of the cup at each of the spectral bands of the CTIS were also obtained [Fig. 27].

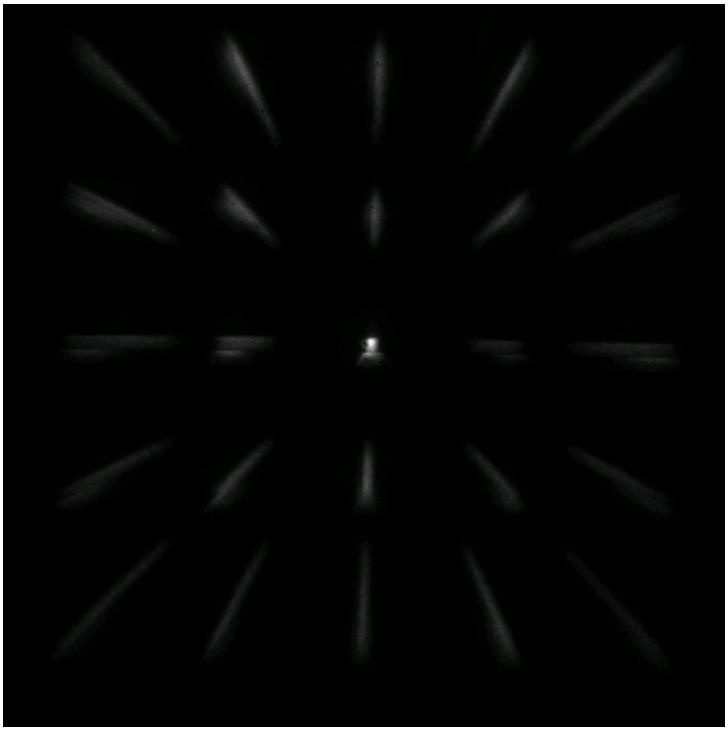

Figure 25: Raw RIS image a coffee cup illuminated with tungsten, fluorescent light bulbs, and a 647 nm laser pointer.

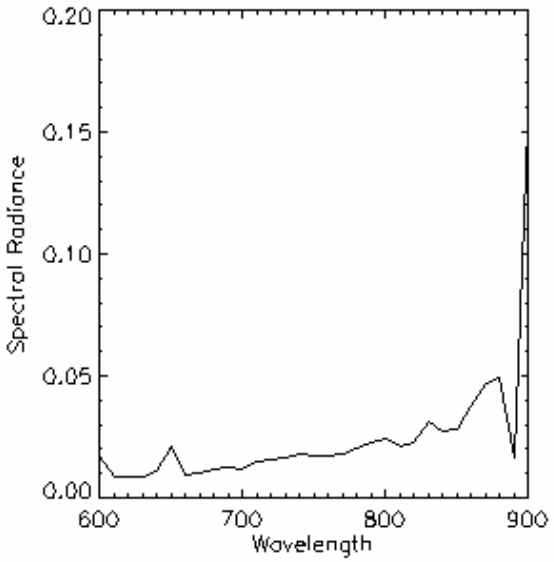

Figure 26: Reconstructed spectra of a single pixel of the coffee cup. This pixel was located where there was illumination from the laser pointer and the 600nm - 900nm with $\Delta\lambda$ = 10nm calibration was used. Note the peak near 650 nm corresponding to the laser line.

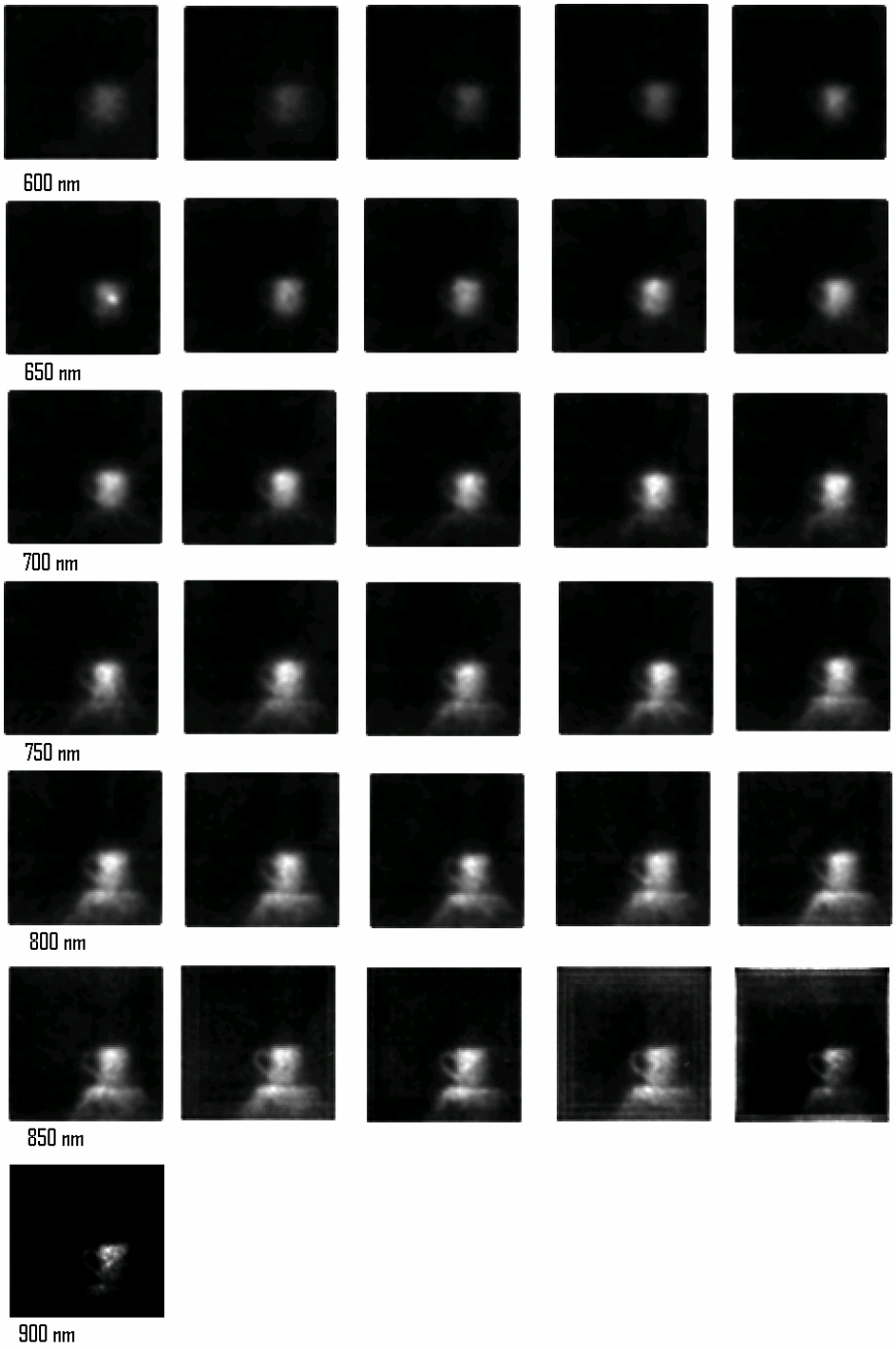

Figure 27: All 31 of the normalized spectral images of the cup. Note the bright spot in the first image of the second row. This is the laser spot at 647 nm contained in the 650nm reconstructed image. This set of images was reconstructed using the 600nm - 900nm with $\Delta\lambda$ = 10nm calibration.

Another spectral test was performed using the same coffee up illuminated with the 647nm laser pointer and with the 857nm laser emitter. The reconstructed spectra of a single pixel in the object where the laser pointer was reflected is shown below in figure 28. What this spectra shows is that we are able to reconstruct the spectra of the object correctly, and that the laser emitter signal is present so we should be able to measure range.

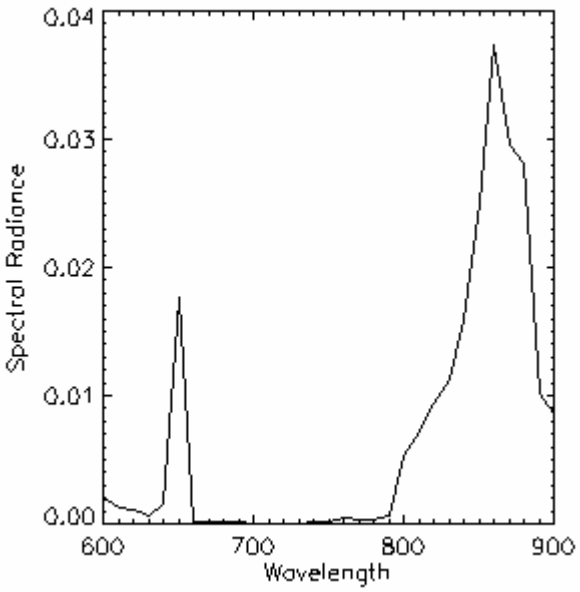

Figure 28: Reconstructed spectra of a single pixel of the coffee cup illuminated with the two lasers. Note the 647 nm peak and the 857 nm peak. Again, there is reconstruction noise in this image at the long wavelengths due to poor calibration images from the 600nm - 900nm with $\Delta\lambda$ = 10nm spectral calibration.

Range Calibration:

The ranging function of the Ranging-Imaging Spectrometer (RIS) is essentially the same as the Scannerless Range Imaging LADAR (SRI LADAR) that Sandia developed (Page 15). The only difference is that range can now be determined only for the panchromatic image contained in the footprint of the 0^{th} order projection, as opposed to the entire focal plane array.

As mentioned before, to determine range, the system floodlight illuminates the scene with laser light (λ = 857nm) modulated at 1 kHz. The reflected laser light is then

imaged onto a gated image intensifier through the CTIS attached to the front of the system. The image generated on the phosphor screen of the image intensifier is then transferred via fiber optic taper to the FPA. The gain of the image intensifier is modulated at 10MHz, and with each successive image, the phase difference between the gain modulation and the outgoing laser pulses is stepped between 0° and 315° in 45° increments. The phase difference between the two waveforms produces a range dependent intensity of the light imaged onto the FPA. As the phase difference changes, so does the intensity of the light. So if the intensity for each pixel on the FPA would be plotted as a function of phase difference, the plot would a sinusoid. The phase of the resulting sinusoid for each pixel is then used to determine the range according to Equation 14 below.

$$\frac{4\pi f_0 R}{c} + \beta_1 - \alpha_1 \cong ATAN\left[\frac{\frac{-\sqrt{2}}{2} I_1 - I_2 - \frac{\sqrt{2}}{2} I_3 + \frac{\sqrt{2}}{2} I_5 + I_6 + \frac{\sqrt{2}}{2} I_7}{\frac{\sqrt{2}}{2} I_1 - \frac{\sqrt{2}}{2} I_3 - I_4 - \frac{\sqrt{2}}{2} I_5 + \frac{\sqrt{2}}{2} I_7 + I_8}\right] \qquad [14]$$

Where R is the range, f_o is the 10MHz modulation frequency of the image intensifier, c is the speed of light, I_n is the image with the subscript denoting the number of the image in sequence, and $\beta_1 - \alpha_1$ is the range calibration matrix.

To range calibrate the system, the range calibration matrix ($\beta_1 - \alpha_1$) must be determined. $\beta_1 - \alpha_1$ is a matrix that is dependent on the field of view of the system [2]. To determine the range calibration matrix, a flat target large enough to fill the field of view of the sensor is placed perpendicular to the optical axis of the system at a known distance. Due to the increased parallax between the laser emitter and receiving optics of the RIS (Page 28), the distance away from the focal plane of the camera that the target can be placed at has to be greater than 160cm. Placing the target at a distance longer than 160cm ensures that the entire field seen by the FPA is illuminated by the laser emitter.

The range calibration target is flat and is composed of Styrofoam. The target was placed at a distance of 2.5m away from the focal plane. Ten sets of phase images were obtained using only light from the laser emitter (no ambient light present) and ten sets of dark phase images were acquired for dark noise subtraction. These two sets of ten

images then averaged and the dark frames were subtracted to improve the signal to noise ratio.

The averaged and dark subtracted phase images are then inserted into the right hand side of equation 14, R is set to 2.5m, f_o is set to 10MHz, and the equation is solved for the calibration matrix $\beta_1 - \alpha_1$. Figure 29 is an image of the calibration matrix; it is scaled to see the detail.

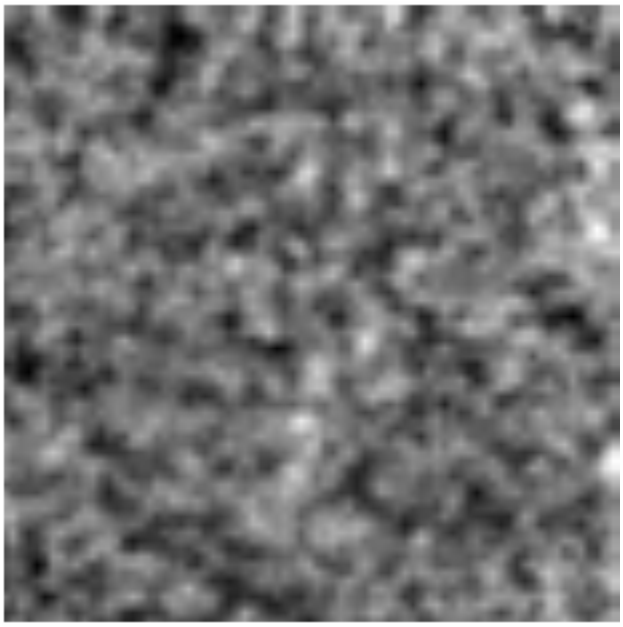

Figure 29: Image of the range calibration matrix $\beta_1 - \alpha_1$.

Verification of the Range Calibration and Range Resolution:

With the range calibration completed for the RIS, the range calibration was then tested for accuracy and resolution. This test was carried out in the lab using two flat Styrofoam targets in a darkened room. The targets were composed of the same material as the range calibration target. The targets were placed side-by-side and perpendicular to the optical axis of the RIS. One target was placed at the calibration distance of 2.5m and served as a reference target. The second target (test target) was moved either closer of farther away from the sensor. This allowed simultaneously testing of the range calibration and range resolution of the sensor.

The separation distances between the test and reference targets was measured as followed: Distances when the test target is closer to the sensor than the reference target,

are negative, and distances when the test target is farther away from the sensor than the reference target, are positive. These distances were ranging from 2.15m to 2.9m (or in the previously described convention -0.35m to +0.40m). A diagram of the test configuration is shown in Figure 30.

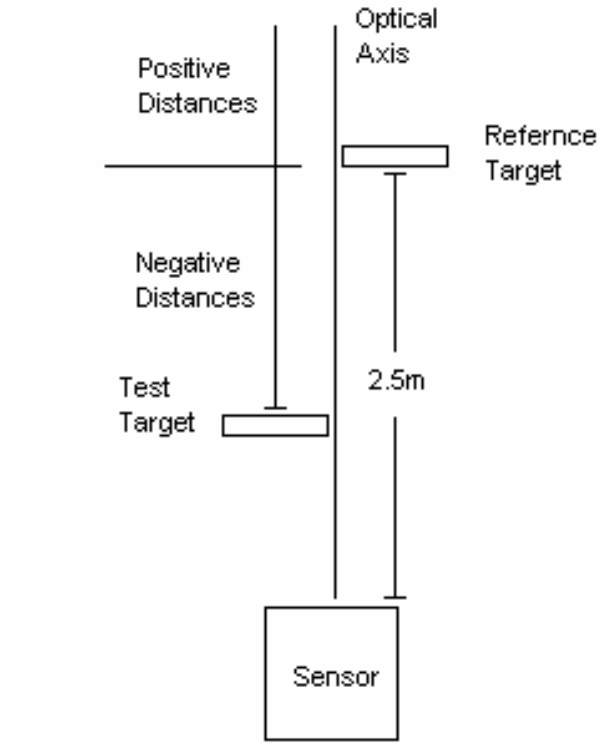

Figure 30: Diagram of the Range Calibration\Range Resolution Test

The test target was moved in 5cm intervals from -35cm to +40cm. Six sets of phase images were taken at each of the positions. Three of these sets were obtained with the laser on, and the second three sets were taken with the laser off. The second set is used to perform a dark subtraction on the data. The three sets of data were averaged and the dark subtraction was performed. An 11 x 11 pixel subsets of the panels was used for the range analysis. Images of that target with a panel separation of +40cm are shown in figure 31. Plots of the averaged range data are shown in Figure 32. The maximum range error is 20cm for a separation distance of +40cm and the rms resolution error is 17.56cm.

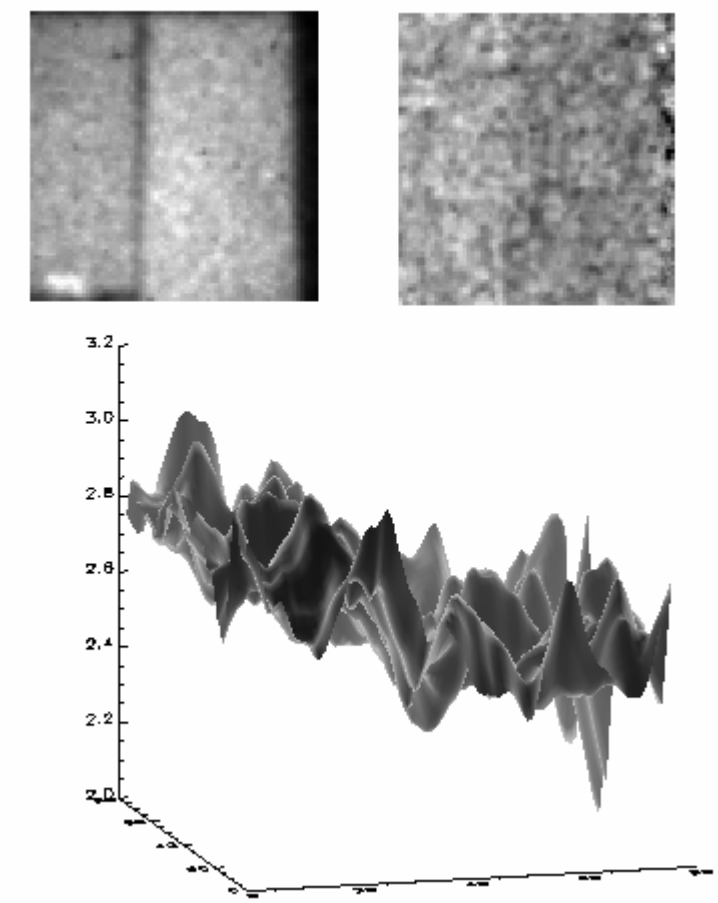

Figure 31: Upper Left: Raw phase data of the +40cm trial scaled to show detail, Upper right: calculated range image scaled to show detail, Bottom: 3-D surface rendering with a 7 pixel boxcar average.

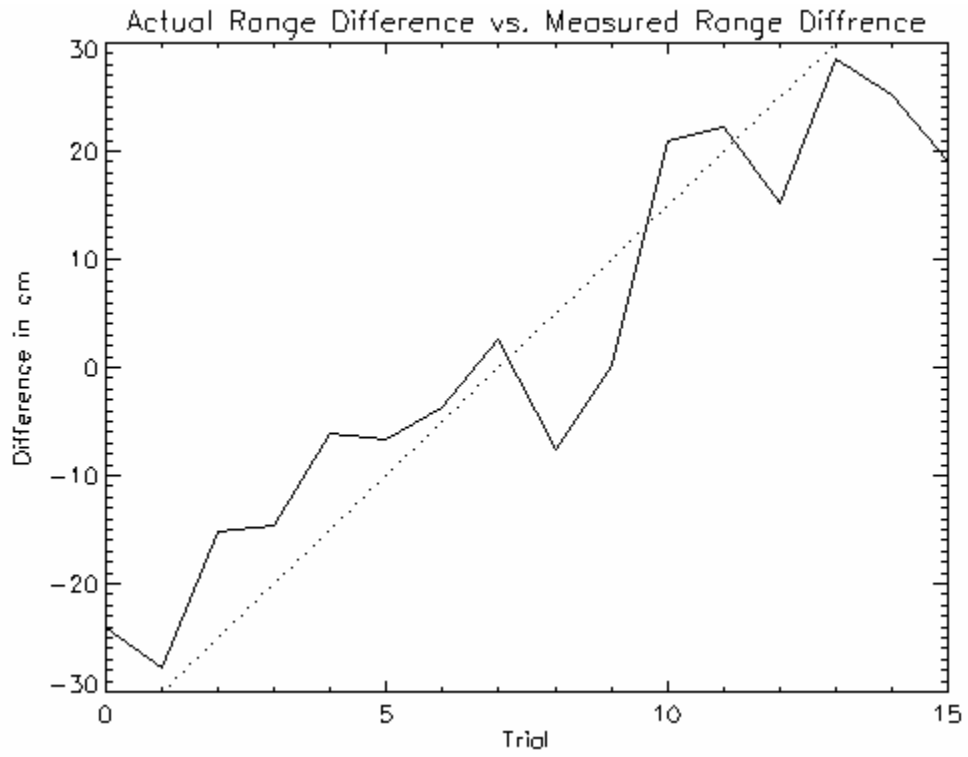

Figure 32-a: Plot of the measured average range difference (solid) and actual range difference (dotted)

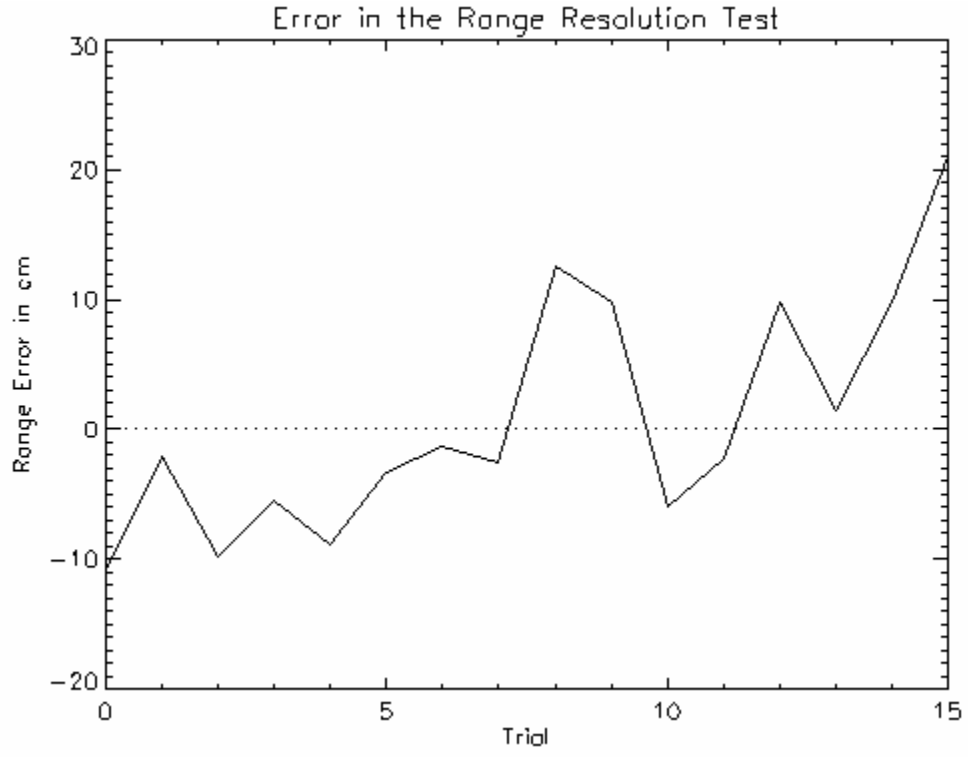

Figure 32-b: Plot of range resolution error

Range verses MCP Gain:

The 10MHz frequency that is used in the heterodyning technique to measure range is applied in the RIS by sinusoidally modulating the gain applied to the micro-channel plate (MCP) of the image intensifier. The only adjustment that can be made to the 10MHz signal is to change the DC offset of the gain. The need to change the offset is dependent on the distance and reflectivity of the target.

An experiment was carried out to see the effect of changing the gain of the MCP on the range reconstruction. The flat Styrofoam target used to calibrate the system was placed at a distance of 2.5m from the focal plane. The target was large enough to fill the field of view of the system. The only light that was incident on the target was the laser illuminator. The voltage range that can be applied to the MCP is from 800V - 1100V. The software used to operate the RIS coverts the voltages to digital numbers (dn) ranging from 0dn – 255dn. The test was ran from 120-220dn in 5dn steps, or from 941.09V – 1058.67V in 5.89V steps. Three sets of phase images were taken at each of the MCP voltage settings and were averaged. No dark subtraction was performed for this test. The averaged phase images were used to construct range frames at each of the MCP voltage settings. An 11 x 11 pixel subset of the range frame was averaged and plotted against the MCP settings. The results showed that there is a slight upward slope to the range as the MCP gain is increased, with the values staying very near the correct distance. A plot of the data is shown in figure 33.

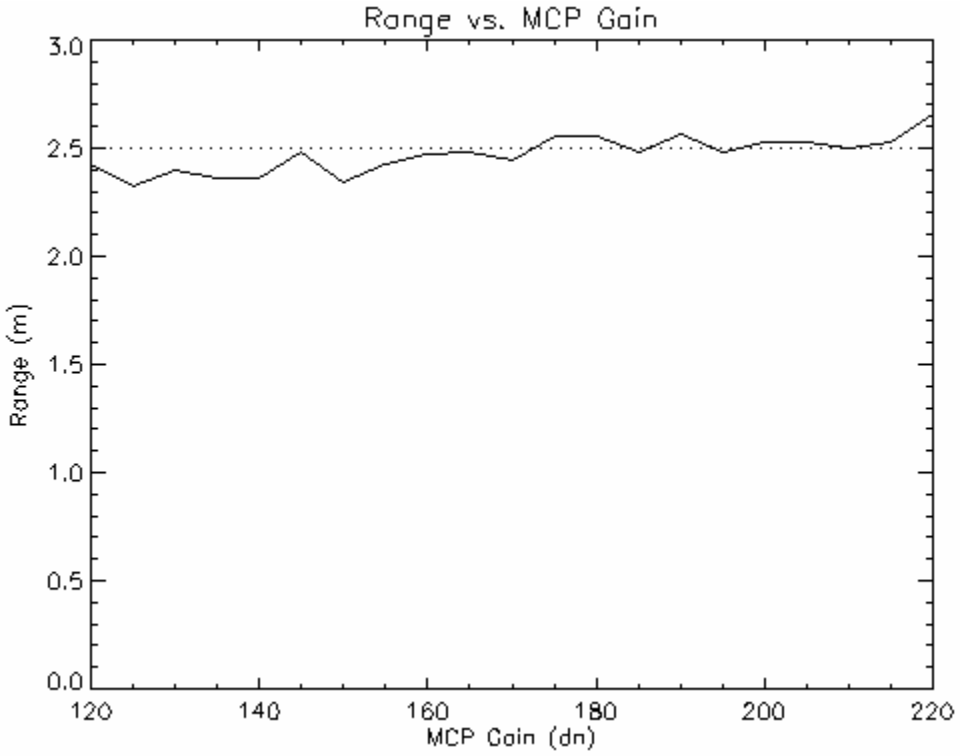

Figure 33: Range verses Micro-Channel Plate gain (dn)

Range versus Ambient Illumination:

As mentioned before, the LADAR contained a narrowband optical filter centered on the laser emitter wavelength. This filter was placed in the receiving optics train to prevent ambient light from entering the system. In order to make the instrument broadband, the filter was removed allowing the spectral measurement of the scene to be made. According to the derivation of the range algorithm [2], it is the phase information encoded in the sequence of phase images that contains the range information and not the intensity of the light. This says that ambient light should not have an effect on the range measurement.

To verify that ambient light should not affect the range measurement, a computer simulation was carried out using actual range data. A flat Styrofoam target was placed 2.5m away from the focal plane of the RIS. The room was darkened to only allow light from the laser emitter to illuminate the target. Ten sets of phase images were collected with the laser on and were averaged. Ten more sets of phase images were collected with the laser off and averaged. This second set of data was subtracted from the first set to

remove dark noise from the camera. The resulting set of phase images was then used in a simulation program that artificially adds ambient light to each of the images in the phase sequence, and then performs the range calculation.

For each of the 200 trials of the simulation, the computer artificially added 5dn of ambient light to each of the images in the phase sequence. The same amount of ambient light was added to each image because the ambient light is assumed to be constant over many periods of MCP gain modulation yielding the same average intensity. A plot of the average intensity of each of the phase images for the entire simulation is shown in figure 34-a. After the computer added the artificial light to the phase sequence, the average range was calculated. A plot of the average reconstructed range versus trial number is shown in figure 34-b.

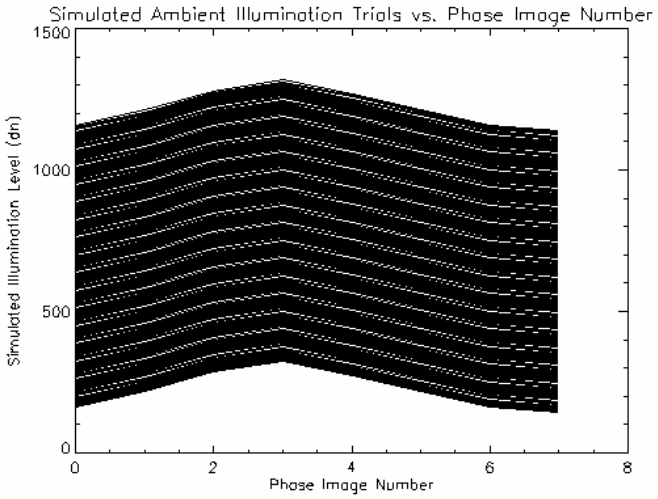

Figure 34-a: Plot of the successive Ambient Light trials verses Phase image number

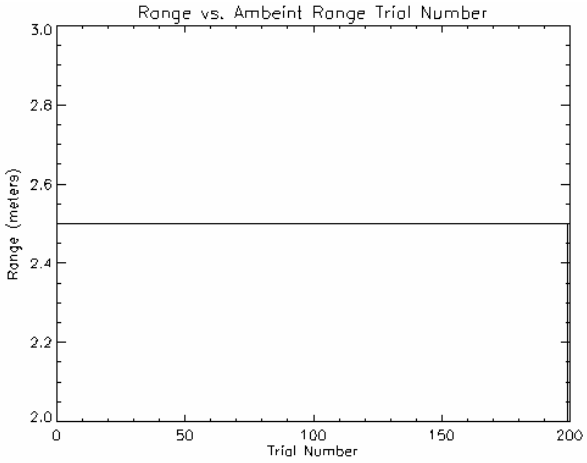

Figure 34-b: Reconstructed Range verses Simulated Ambient Light Trial

As can be seen in figure 34-b, the range was calculated to be 2.5m for each trial. This proves that ambient light should have no effect on the range calculation. The ambient light affect was then tested in the lab.

To test the effect of ambient light on the RIS, a target was placed at a distance of 2.5m away from the FPA of the sensor. A 250W projector-type light bulb was used to floodlight illuminate the target. The light bulb was powered by a variable output DC source to eliminate the 60Hz AC signal. A broadband UDT detector was placed near the objective lens of the system to record the level of the ambient light. To change the amount of ambient light, the current through the light bulb was adjusted using the DC source.

Twenty-eight different ambient light levels were measured during the experiment. The first trial contained no ambient light and the 28^{th} yielded $11.65 W/m^2$ incident on the RIS. During the test, the current applied to the bulb was increased non-uniformly until a difference in illumination was noticed by the human eye. The difference in illumination was noticed at trial number 10, and from that point the ambient light was increased linearly. A plot of the ambient light level verses trial number is shown is figure 35.

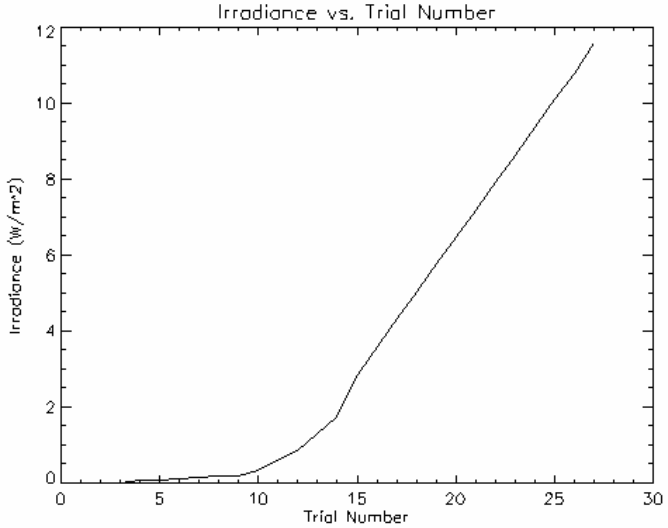

Figure 35: Plot of Ambient Light Level verses Trial Number

During the experiment two types of phase sequence images acquired. The first types of images contained both the laser and ambient light and are referred to as 'laser' phase images. For the second type of phase images, the laser emitter was blocked so they

contained only the ambient light and are referred to as 'ambient' phase images. Three sets of each type were taken and averaged at each of the ambient light levels.

The range was calculated for each of the ambient light levels for the laser phase images only. The ambient phase images are not modulated and do not contain any range information. The range images were examined using 11 x 11 pixel subset where the illumination was fairly uniform. In figure 36, a plot of the range verses ambient light is shown. It can be seen from the graph that the ambient light does have an effect on the range, disagreeing with the simulation.

To help correct this error in the range reconstruction, the ambient light phase frame was subtracted from the laser phase frame, leaving only the laser light present. This procedure improved the range reconstruction at low ambient light levels. However, it overcorrected the range at high ambient light levels, as shown in figure 37.

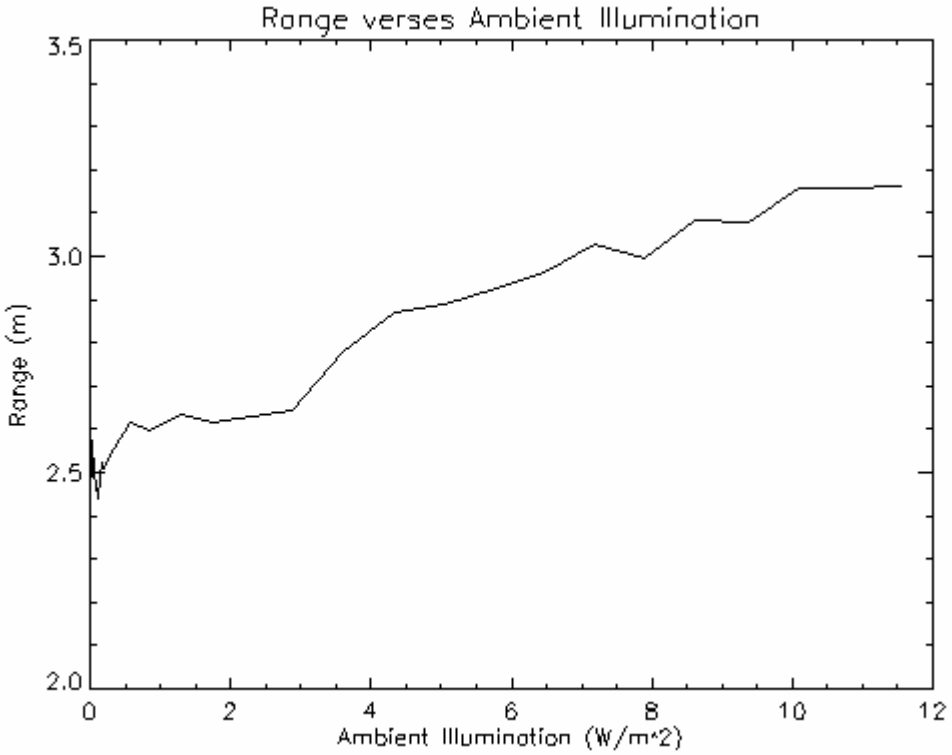

Figure 36: A graph of Range verses Ambient light level

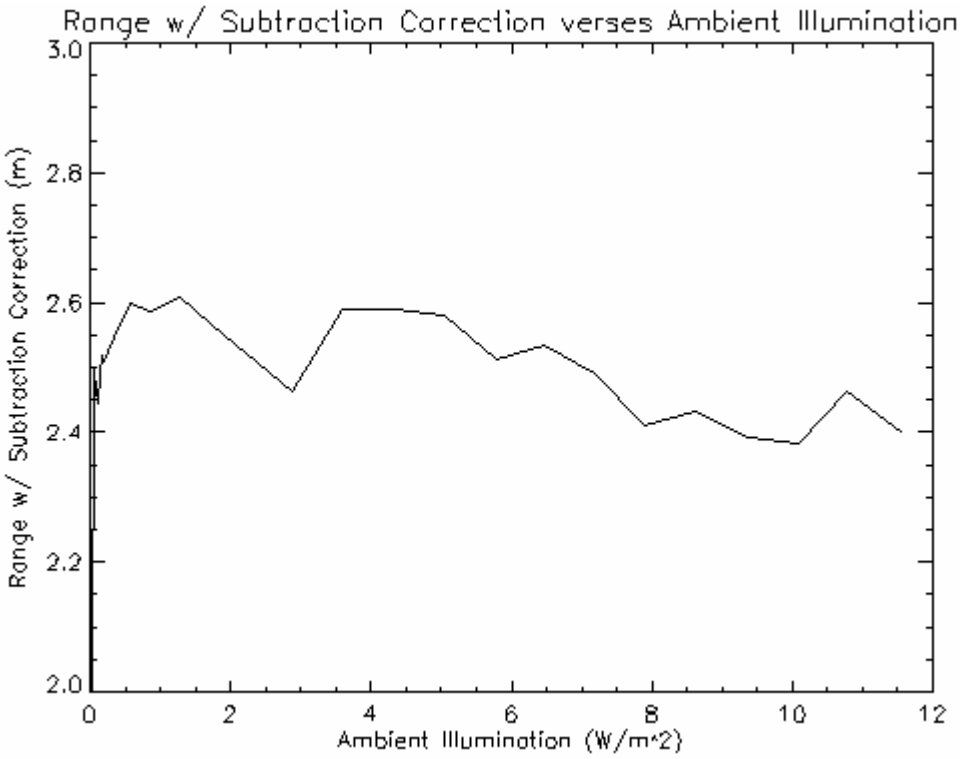

Figure 37: Plot of Range verses Ambient Light Level with the Ambient Subtracted Data

From the analysis of the graphs above and with the ambient light simulation that was previously performed, it was concluded that a non-linear, signal dependent noise process in the camera that is contributing to the error in the range reconstruction. This noise is most likely contributed to the response of the image intensifier.

Variance Shaping Correction:

Examining the statistics of the phase images (Figure 38) it was shown that the mean pixel value has a linear relationship with the ambient light level. However, the variance of the pixels value distribution has a non-linear relationship with the ambient light level. It was our belief that at large ambient light levels, this non-linear relationship breaks down the assumptions that the range equation (Eq 14) is based on, causing errors in the range reconstruction algorithm.

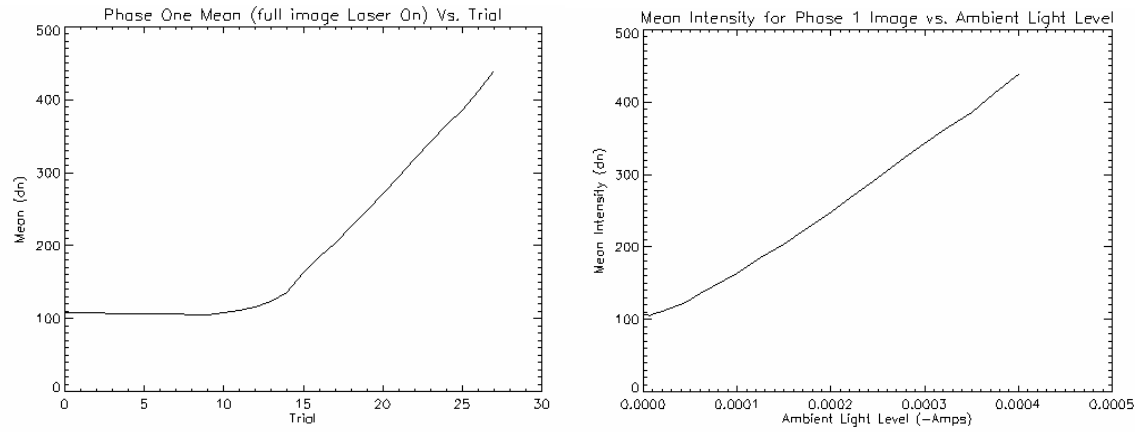

Figure 38-a: Mean of the first phase image versus trial number and ambient light level.

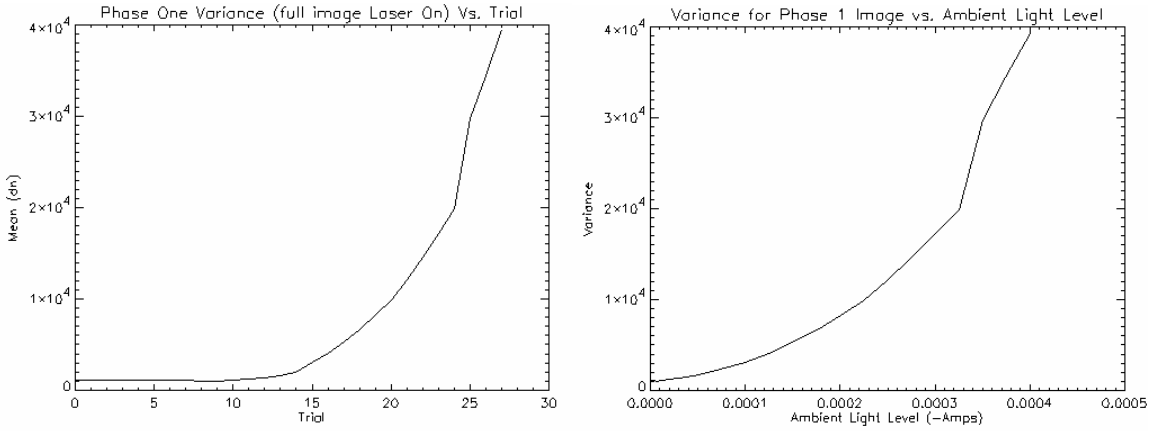

Figure 38-b: Variance of the first phase image versus trial number and ambient light level.

From figure 38 it can be seen that the mean intensity of both the laser and ambient phase images has a linear relationship with the ambient light level. This suggests that if we take two sets of data, laser phase images and the ambient phase images, and subtract them, the resulting phase frame would have the same value for the mean in each of the images as if the data would have contained only light from the laser emitter.

For each of the ambient light levels, the ambient phase frame was subtracted from the laser phase frame (these types of phase frames are referred to as subtracted phase frames). The mean of the resulting data for the first image in the phase sequence (phase 1) was plotted against the ambient light level in figure 39. A reference line of the mean frame value for data containing the laser only is included in the graph as a reference.

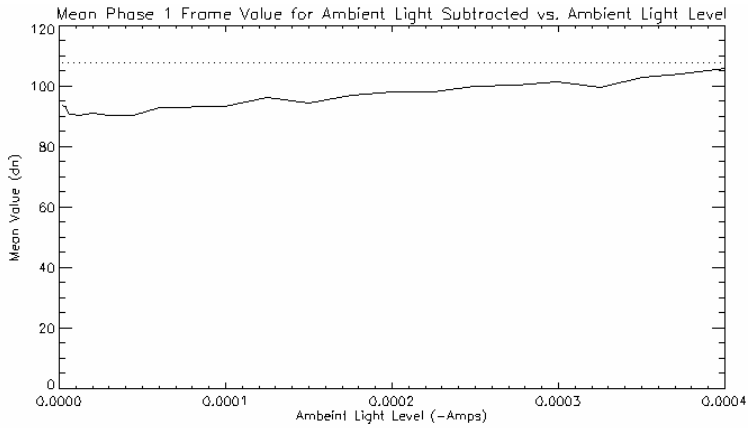

Figure 39: Mean phase 1 values for ambient light subtracted data versus ambient light level with average laser only reference line.

It can be seen from the graph in Figure 39 that the average values of the first phase frame of the subtracted phase sequence is below the mean value of the mean laser phase frame for each for the ambient light levels. However, if we then subtract the value of the average dark noise from the average laser phase frame value, and use that as anew reference for the subtracted phase plot (Figure 40). We see that the average subtracted phase frame value agrees with the average dark noise subtracted laser phase value. This shows that subtracting the ambient phase images from the laser phase images also removes the dark noise contained in the camera and is independent of the ambient light intensity.

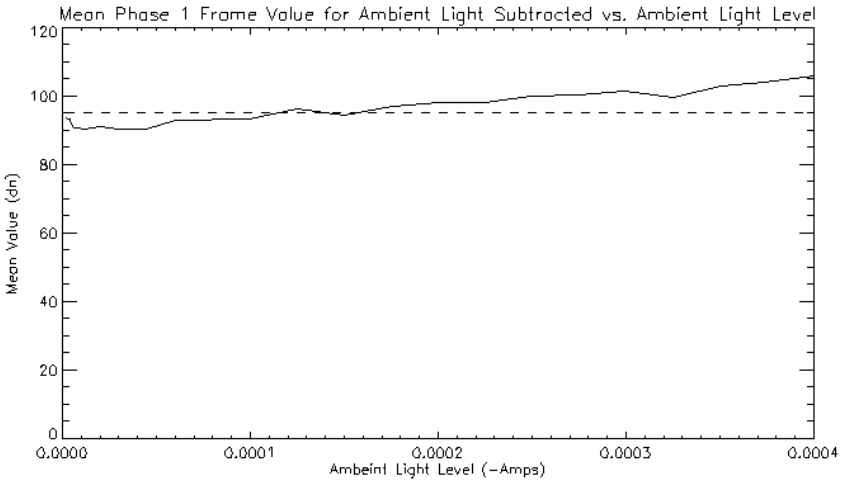

Figure 40: Mean phase 1 values for ambient light subtracted data versus ambient light level with the dark subtracted average laser only reference line.

Examining the pixel distributions at each of the ambient light levels, it was found that the distribution of pixel values is normal. It is also confirmed that as the intensity of the ambient light increases, the variance also increases nonlinearly as can be seen in Figure 38. The increase in the variance of the pixel distribution shows that there is signal dependent noise in the focal plane array.

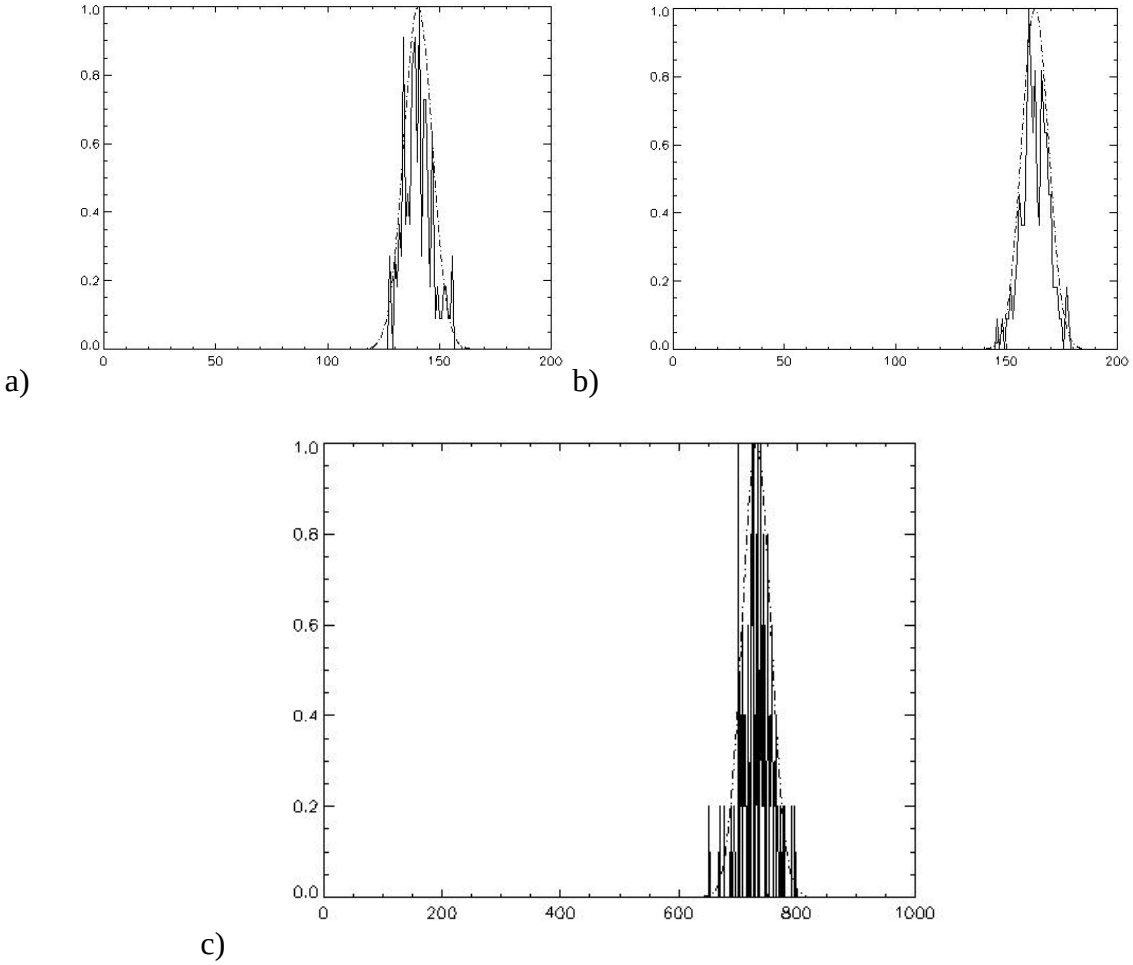

Figure 41: Plots of phase 1 pixel distribution with a Normal distribution overlay (dotted line) for three different light levels a) 0W/m^2 b) 4.85 W/m^2 c) 11.65 W/m^2.

This increase in the variance of the images is responsible for the increase in the reconstructed range value as a function of ambient light level (Figure 36). When the ambient phase frames were subtracted from the laser frame creating the subtracted phase frames, the difference in the variance of the images caused the downward slope in the reconstruction (Figure 37).

This error can be corrected by redistributing the pixel values into the desired distribution. Since the probability distribution of the pixel values is normal, they can be expressed as a function of another random variable using equation 15 [7].

$$P_x(x)dx = P_y(y)dy \qquad 15]$$

where P_x and P_y is the probability distribution function of the random variable x and y respectively, and y = f(x). Since P_x is known, we can rearrange Eq 15 and solve for P_y in terms of P_x and x yielding Eq 16.

$$P_y(y) = P_x(f^{-1}(y)) * \frac{dx}{dy} \qquad [16]$$

Implementing equation 16 into the computer can be difficult; in this case it is straightforward because the distributions are normal. The desired distribution can be found from the measured data, multiply by the ratio of the desired standard deviation to the measured standard deviation, so that solving for y we get:

$$y = ((x - \bar{x}) * \sqrt{\sigma_y^2 / \sigma_x^2}) + \bar{x} \qquad [17]$$

Where y is the desired pixel value, x is the measured pixel value, $\bar{x}$ is the mean of the measured distribution, σ_y^2 is the variance for the laser illumination only (desired variance), and σ_x^2 is the measured variance. The desired variance was found by taking a phase image of the target illuminated only with the laser light and calculating the variance of the pixel distribution.

This variable transformation, hereafter referred to as variance shaping, was carried out for all of the ambient illumination levels and is shown in Figure 42 and 43. The range reconstructions using the variance shaping technique improved the measurement by up to an average of 3.1cm over the subtraction technique (Figure 42). In comparison for using no correction technique, the variance shaping of the data improved the average reconstructed range by a factor of 10 from 26cm to 2.6cm

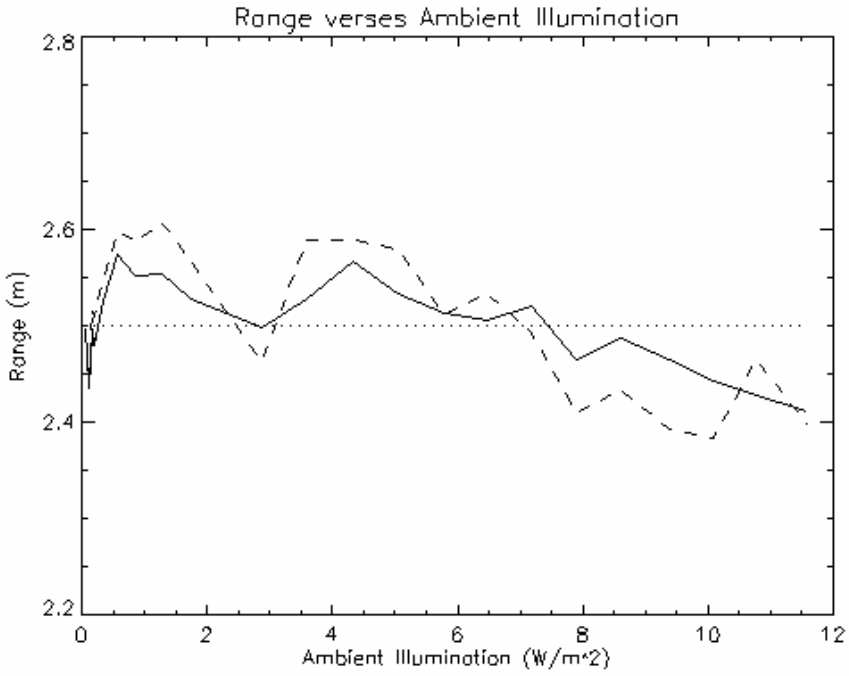

Figure 42: Plot of range verses ambient light, the solid line is the variance shaped data, the dashed line is the ambient light subtracted data, and the dotted line is a reference line of the actual distance.

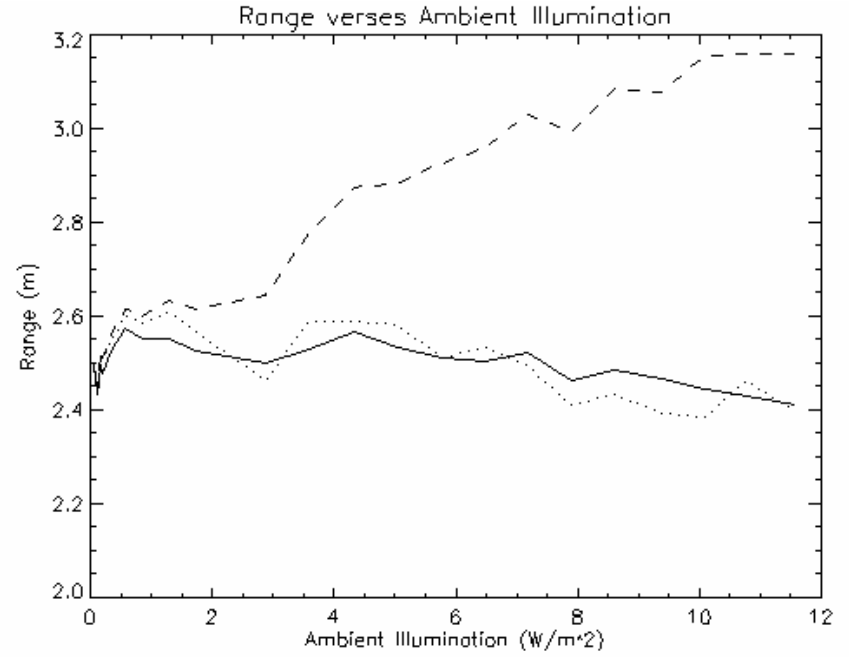

Figure 43: A plot of range verses ambient light level, the solid line is the variance shaped range, the dotted line is the subtracted range, and the dashed line is the ambient range.

Field Test: The system was transported outside where it could be tested under natural light. The system was set up in a shaded area and Styrofoam targets were arranged in two different configurations: Configuration A is a single target at a range of 4.88m, and Configuration B has two targets, one at 4.27m and the second at 6.40m.

Configuration A was the first to be tested. The first set of phase images taken with the camera saturated the pixels so the aperture was stopped down. Four images were then taken in this configuration. Two of the images had the laser blocked so the ambient light subtraction can be performed.

Configuration B was then tested with the system stopped down as well. Again, four images were taken, with two of them with the laser blocked. After this test the system was transported back into the lab and the images were processed.

The system was returned to the lab and the images from Configuration A were processed first. A large dark strip appeared at the top, covering over 50% of the image. This dark strip occurred because the image has shifted on the focal plane with respect to the calibration images. This can only occur from an alignment error. It is our belief that vibrations encountered during transportation caused the shift. The optical mounts were checked by hand to see if any of them became loose. After inspection none of the mounts were loose, so it is our belief that something internal to the LADAR has moved. At the time of this report the cause of the shift has not been determined. Figure 44 and 45 shows the shift of the reconstructed spectral images.

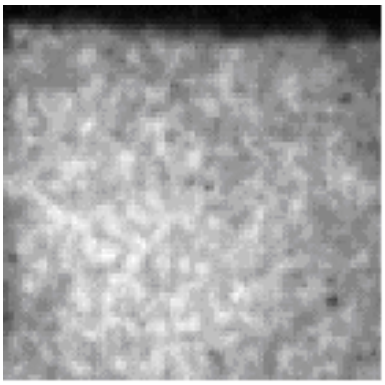

Figure 44: Image before the system was transported for field tests

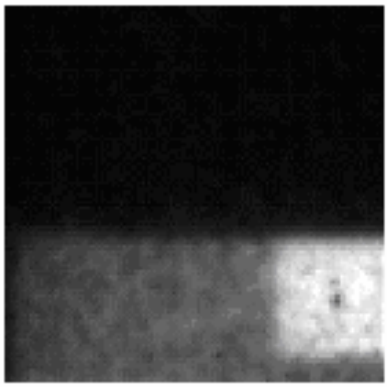

Figure 45: Image after the system was transported for field tests.

There are several methods to correct for the shift. One method to correct would be to realign the optics to move the image back to the center of the focal plane array. Another possibility is to recalibrate the system for the new position. Both of these techniques are time consuming and exhaustive. The simplest method is to use the shift-invariant assumption and translate the images in the computer back to where they should be. The translation method is valid if no part of the diffraction pattern has fallen off of the focal plane. Once the images were shifted back into position, they can be reconstructed without loss of spectral information. Since no part of the diffraction pattern has fallen off of the array the translation technique was used for the remainder of the project.

The shifting of the image also caused problems for the range software. The software we designed to grab a specific window in the full image captured on the array. This window of data originally contained only the 0^{th} order. Once the image shift occurred, the window no longer contained all of the 0^{th} order of the diffraction pattern. The problem for the range software was also corrected using the shift-invariant assumption. The values that told the computer where to grab the window were changed to the values describing the new location of the 0^{th} order.

System Performance Tests:

The following tests were carried out on the system to analyze the spectral and range capabilities of the instrument.

Range Tests

The purposes of the range tests are to investigate the ranging properties of the instrument including: Range Linearity, Lateral Resolution, and Detecting Natural vs. Manmade objects. Each of these tests is presented below.

Range Linearity: This test is to verify the linearity of the ranging portion of the system. As a target gets farther away from the sensor, the signal-to-noise (S/N) ratio decreases which then can lead to reconstruction errors. A test was carried out in the laboratory using a Styrofoam target where the target-sensor distance can be varied. The target was illuminated only with the light from the laser emitter at 857nm. The target was initially placed 6ft away from the sensor and moved back in 1 foot increments until it reached 20ft. When the target was at 20ft, the S/N on the computer display was too low to discern the target from the background. Three sets of phase images were taken at each of the distances and averaged.

The target was originally built to fill the entire field at 2.5m, since it was used at all of the range positions, it did not fill the entire field of the instrument at longer distances. Therefore, an 11 x 11 pixel subset of the data is averaged and used for the analysis. Figure 46 contains a plot of the average range verses actual distance. From the graph it can be seen that as the range increases, the average measured data value begins to fall slightly under the actual distance. Figure 47 shows the S/N ratio verses range for the experiment. We see in figure 47 that as the range increases, the S/N ratio drops from about 17 to 6. It can also be seen in figure 47, a sharp decline in the S/N ratio when the target was at distances greater than and equal 9ft. The distance where the S/N ratio drops is the same distance in figure 46 where the measured range begins to be smaller that the actual range. We concluded that the lowering of the S/N ratio was causing the reconstructed range error. The average measure range error during this test is 1.15ft.

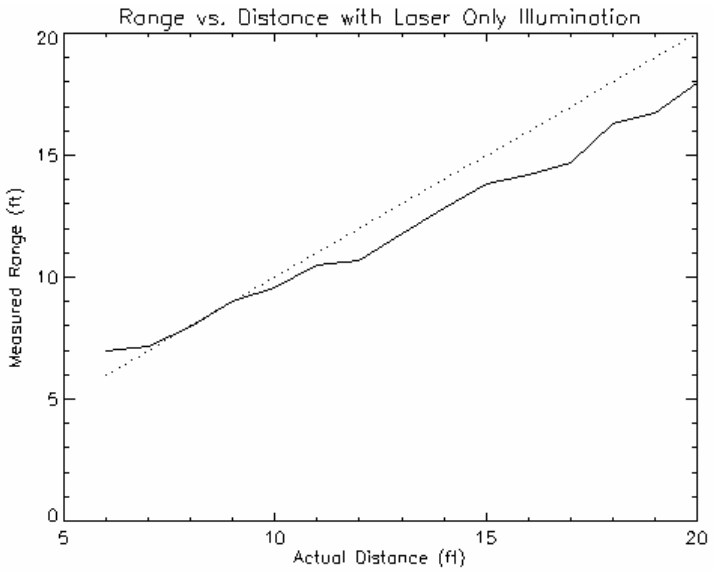

Figure 46: Range verses Distance with Laser only illumination, the actual distance is the dotted line.

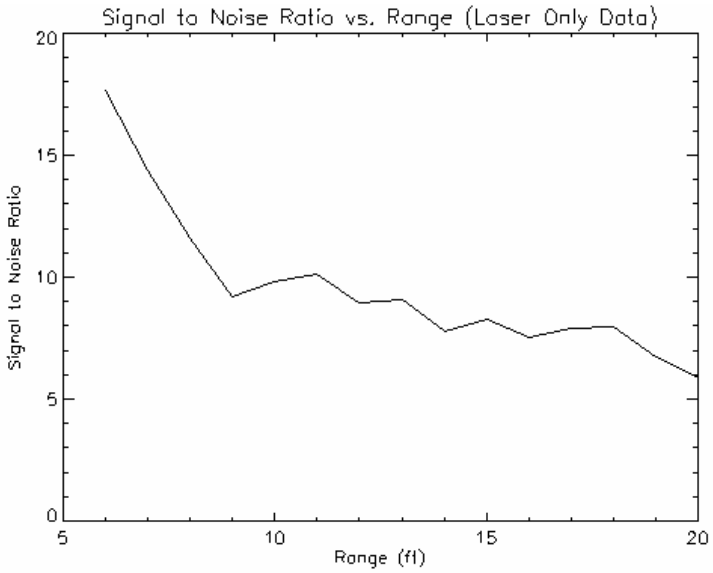

Figure 47: Signal to Noise Ratio verses range with laser only illumination. The result shows that the range calculation is linear with distance. The SNR does affect the calculation but it is near the point were the system is unable to make a measurement.

Natural vs. Manmade: This test placed two manmade objects covered with plants in front of a reference panel made of Styrofoam. The two manmade targets are landmines and they are covered with Oleander and Olive Tree branches. The front of the landmines are placed 30.48cm in front of the Styrofoam target and a total of 2.413m the front of the

instrument. Ten phase image sequences were taken of the target and averaged under the following illumination conditions: Laser only, 2) Laser and Ambient, 3) Ambient only.

This test was performed to verify if the smooth surfaces of the mines could be detected next to the rough surface of the leafy branches. The test scene and its reconstructed range images are shown in Figure 48.

a)

b)

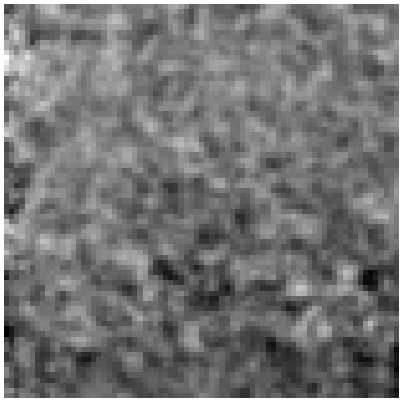

c)

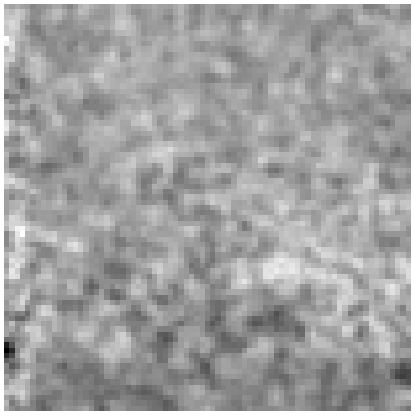

Figure 48: a) Photograph, and range images of the target under b) Range reconstruction for laser only illumination and c) Range reconstruction for laser and ambient illuminations (Range images are scaled to show the detail).

It is very difficult to see any detail in the range images due to the systems range resolution (17.5 cm) combined with the low spatial sampling of the system. But in calculating the average range (over a 5 x 5 pixel subset), we find that the Styrofoam target is 30.4cm behind the mines. The averaged distances are shown in table 2.

Target in Scene	Average Range Laser Only	Average Range Laser and Ambient
Large Mine (66 pixel avg)	2.382m	2.487m
Styrofoam Bkg (121 pixel avg)	2.637m	2.791m
Depth between targets	25.5cm	30.4cm

Table 2: List of the average range distances for difference portions of the target.

a) 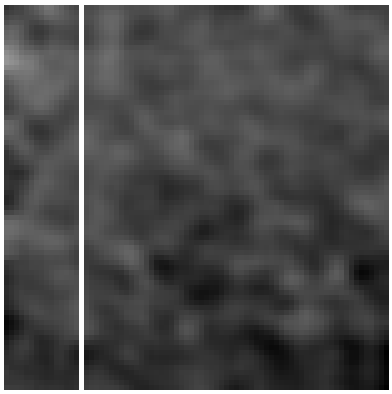 b) 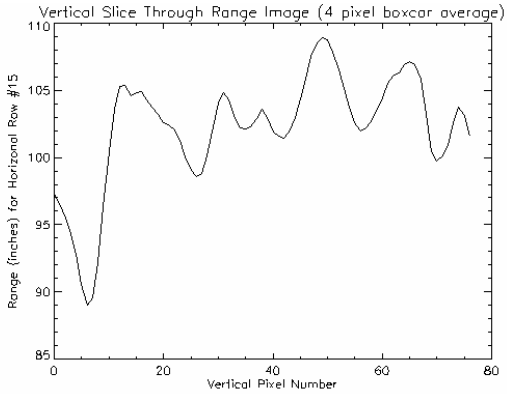

Figure 49: a) 4-pixel boxcar average of laser only range data showing the line that is plotted. b) Range plot of Laser only data with a 4-pixel boxcar average.

What can be seen in the graph in figure 49-b is the definite step between the landmines and the Styrofoam background given by the sharp dip near pixel number 6 on the left hand side of the plot.

Lateral Resolution:

This test was performed to see the affect of the CTIS optics on the lateral resolution of the LADAR instrument. Here we are measuring the edge spread function for the reconstructed range data. A target was placed at a distance of 3m from the sensor. The target (Figure 50) contained a step of 10 inches or 25.4cm in the middle section.

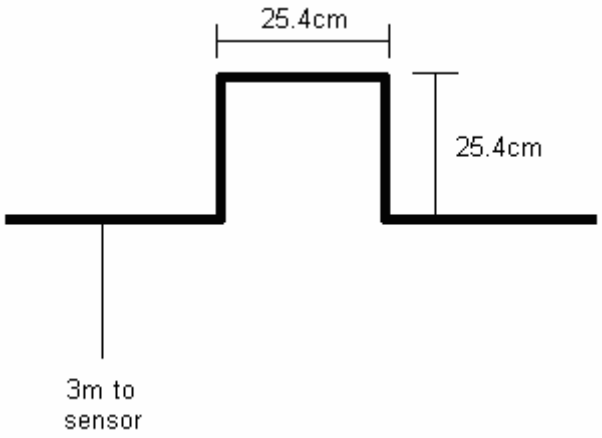

Figure 50-a: Drawing the target used in the lateral resolution test.

a) 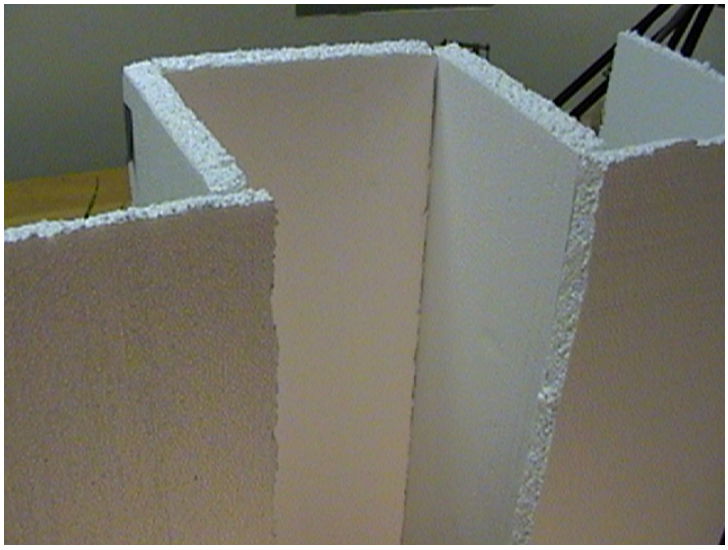

Figure 50-b: Photograph of the target used for the range resolution test.

10 phase sets were taken and averaged of the target in two different positions 1) With step in the Center and 2) With step near the field edge and averaged. Both of the positions were taken with the Laser only, Laser and Ambient, and Ambient only illuminations schemes. First, the data was taken with the CTIS in place. The CTIS was then removed, and the objective lens of the CTIS was placed on the front of the LADAR.

Without the CTIS in place, the entire focal plane of the LADAR contains range information. The LADAR was then recalibrated for range over the entire focal plane, using its full resolution.

To ensure an accurate measure of the lateral resolution, the distance between the LADAR and sensor was adjusted so that the same numbers of pixels were across the step for the two measurement cases (With CTIS and Without CTIS). Data is presented verses values of field percent (i.e. the optical axis is at 0% field height and the very outside edge of the array is at 100% field height. The following figures (Figures 51 and 52) and Table 3 contain the reconstructed images and data respectively. The data presented for this test is the average range across 5 horizontal lines in the reconstructed range image.

a) 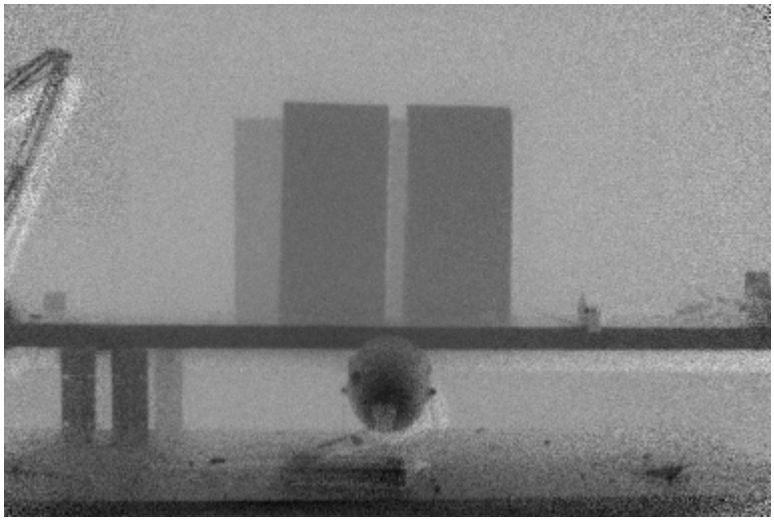

b) 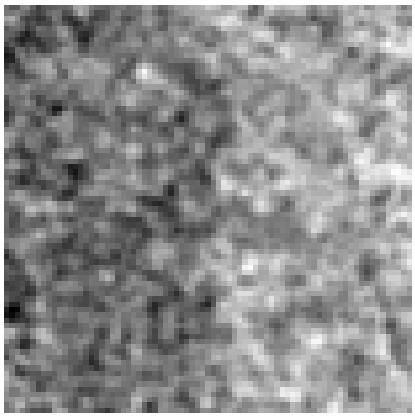

c) 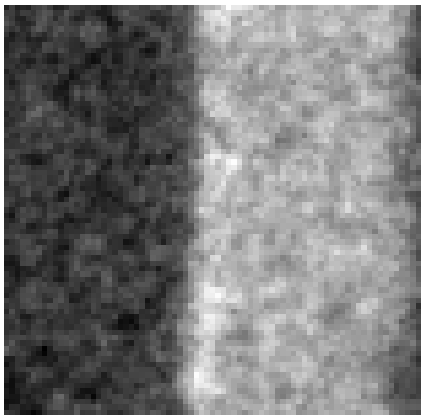

Figure 51: a) Range image of the target on-axis using the without CTIS b) Range image of the target on-axis Laser only with CTIS. C) Range image of target on-axis without CTIS with the same spatial sampling as RIS.

d) 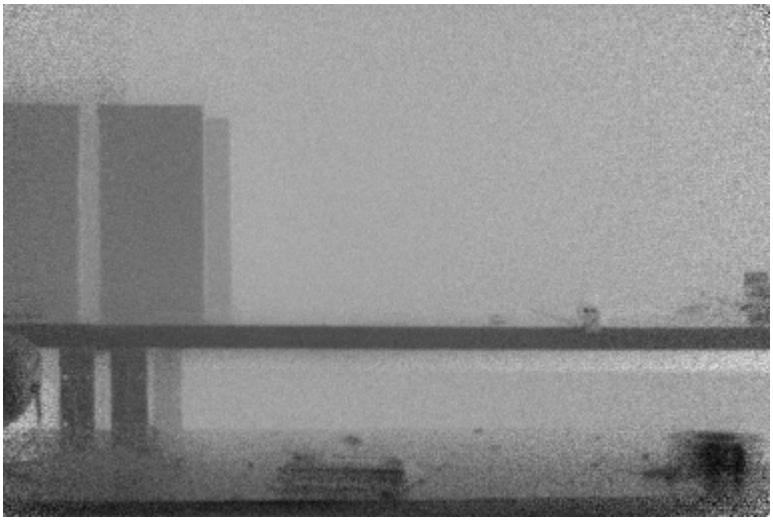

e) 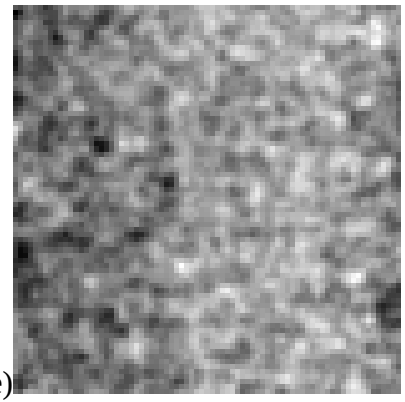

f) 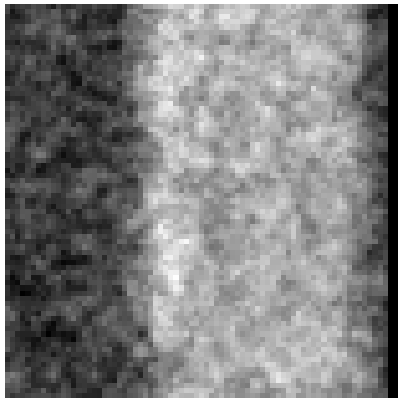

Figure 51: d) Range image of the target off-axis using the without CTIS e) Range image of the target off-axis, Laser only with CTIS. f) Range image of target off-axis without CTIS with same spatial sampling as RIS.

From the images in Figure 51 it can be seen that the CTIS does have an effect on the resolution of the instrument. In figure 52, plots of single lines that cross the step for the on-axis test with and without the CTIS are shown. It can also be seen from these images that the CTIS does have an effect on the edge spread function. The decrease in lateral resolution arises from aberrations contained in the CTIS optics.

Table 3 contains the data pertaining to the number of pixels that occur across the step and the average ranges of the calculated distances from the range reconstruction. For the on-axis measurement the number of pixels across the step more than doubled from 10 pixels without the CTIS, to 23 pixels with the CTIS. For the off axis measurement of lateral resolution, the number of pixels across the edge without the CTIS was 22. For the

off-axis measurement with the CTIS in place, the number of pixels could not be determined because of the low spatial sampling when the step is located at the edge field.

In order to have the same number of pixels across the step portion of the target, the target and sensor had to be positioned for the two different fields of view. The distance between the near/far portions of the target and focal plane of the instrument were 299.7cm/325.1cm and 274.3cmin/299.7cm for the test with and without CTIS respectively. It can be seen from the table that the average range was also more accurate without the CTIS in place. The on-axis absolute range errors for the near/far portions of the target are 12.08cm/14.69cm and 3.55cm/1.62cm with and without the CTIS respectively. The off-axis measurements for the test with the CTIS in place are inconclusive because of the low spatial sampling with the CITS in place. It was concluded from this experiment that the addition of the CTIS reduced the on-axis lateral resolution by 67%.

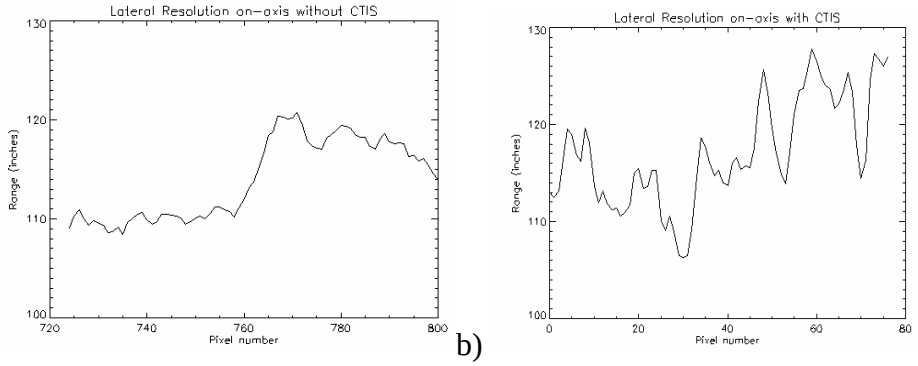

b)

Figure 52: Plot of a single line across the step on-axis, a) without the CTIS, b) with the CTIS.

Test	Pixels Across Edge	On axis Field %	Pixels Across Edge	Edge Field %
With CTIS	23	2.5%	To poor resolution	80%
Without CTIS	10	0.52%	22	81.33%
Average Range	On-Axis Near	On-Axis Far	Off-Axis Near	Off-Axis Far
With CTIS	287.62cm	310.41cm	N/A	N/A
Without CTIS	277.85cm	301.32cm	278.57cm	289.03cm

Table 3: The data for the lateral resolution test.

Spectral Tests

The purpose of the following spectral tests is to verify and examine the spectral capabilities of the RIS. The results of these experiments were compared to a fiber optic spectrometer from Ocean Optics. The following tests were performed using the 597nm – 807nm with $\Delta\lambda$ = 5nm spectral calibration:

Spectral Resolution:

The spectral resolution test investigates the ability of the Ranging-Imaging Spectrometer to resolve spectra. A target was created using a Styrofoam background and had several LEDs imbedded in it. The LEDs were from the company Cal-Pak, the product number and peak wavelength of the two LEDs used during the test are shown in table 4. The peak wavelength of the LEDs was measured using an Ocean Optics spectrometer.

Cal-Pak LED Number	Peak Wavelength
Cal-Pak 5	642.636nm
Cal-Pak 41	623.566nm

Table 4: List of LEDs used in the spectral resolution test.

These two LEDs were chosen because they had the closest peak wavelengths that were available at the time of the test. The LEDs were placed as close as possible in attempt to have them imaged onto a single pixel. Due to the low intensity of the LEDs; the target had to be placed closer to the sensor than desired (3m) causing them to extend spatially over several pixels. Tests were taken with and without the laser emitter illuminating the target with either one or both of the LEDs. The results of the reconstructed spectra obtained with RIS are compared to the reference spectrometer measurements.

The first set of tests had only one of the two LEDs illuminated. The reconstructed spectra are shown in the following figures (Figures 53-54) with the reference spectra measurement superimposed as a dotted line.

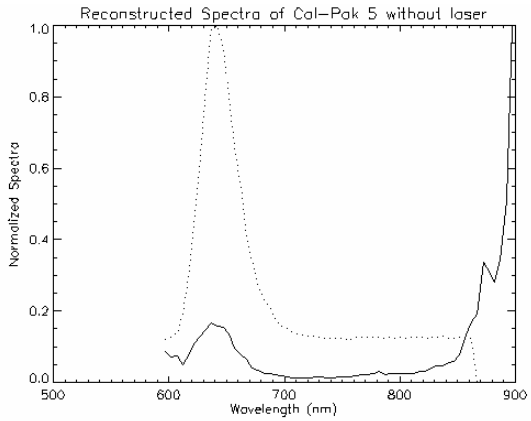

Figure 53: Plot of Cal-Pak 5 LED spectra (peak at 642.636) Illuminated without laser emitter (857nm), obtained with 10 iterations of the MART algorithm, overlaid with reference spectra (dotted line).

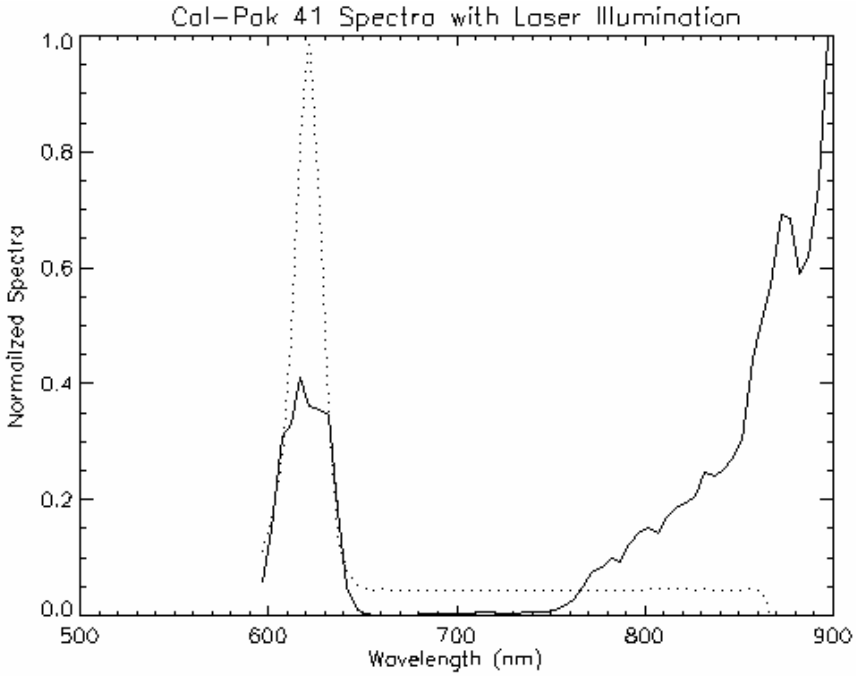

Figure 54: Plot of Cal-Pak 41 LED spectra (peak at 623.566nm) Illuminated with laser emitter (857nm), obtained with 5 iterations of the MART algorithm, overlaid with reference spectra (dotted line). The data was thresholded to remove dark noise.

It can be seen from figures 53 and 54 that the RIS is able to detect the peak of the two LEDs with and without the laser emitter firing.

The next test had the two LEDs, 623nm and 643nm, simultaneously turned on and located next to each other on the Styrofoam target. Again, these two LEDs were chosen because of the separation of their peaks being only 19.08nm. It would have been advantageous to have the spectral peaks closer because Nyquist sampling determines the spectral resolution of the sensor with this calibration to be 10nm. However, this combination of LEDs had the smallest spectral peak separation available at the time of the experiment.

The spectra were then reconstructed using 10 iterations of the MART algorithm, and the results are shown in the following figures (Figures 55-57). From the figures it can be seen that the RIS was able to resolve the two peaks of the test target with (Figure 56) and without (Figure 57) the laser emitter on.

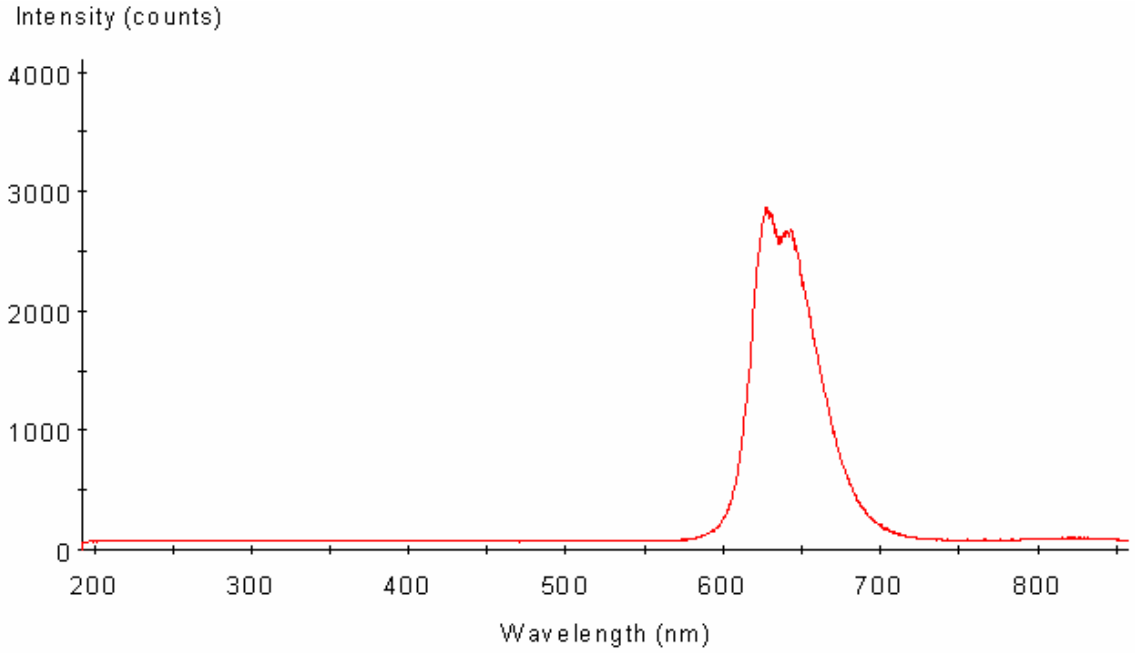

Figure 55: Reference spectra of Cal-Pak 5 and 41 LEDs without laser taken with Ocean Optics spectrometer.

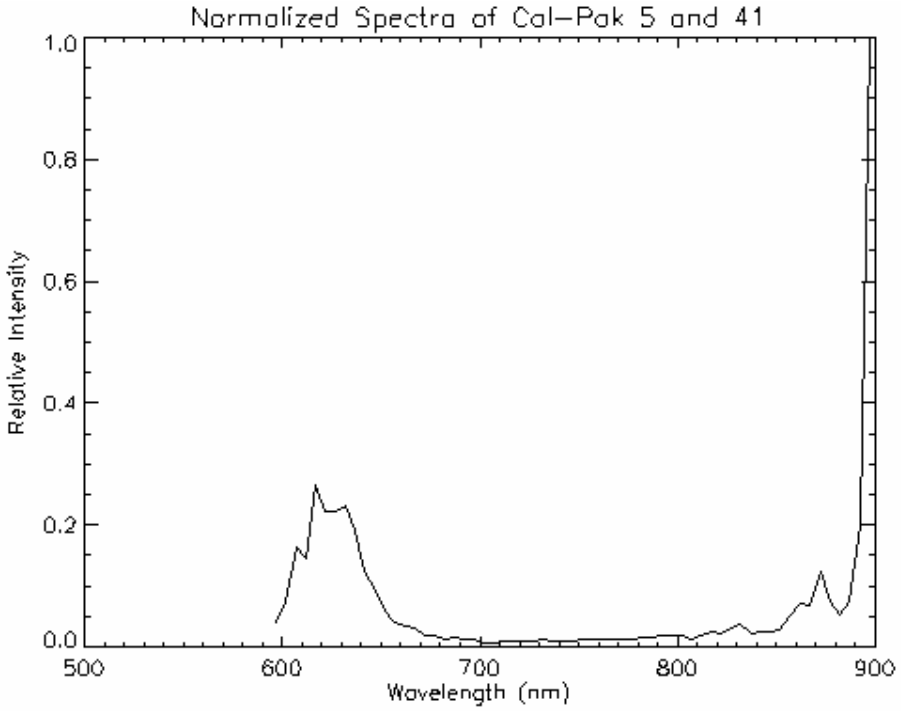

Figure 56: Normalized spectra of Cal-Pak 5 and 41 LEDs without laser reconstructed using 10 iterations of MART.

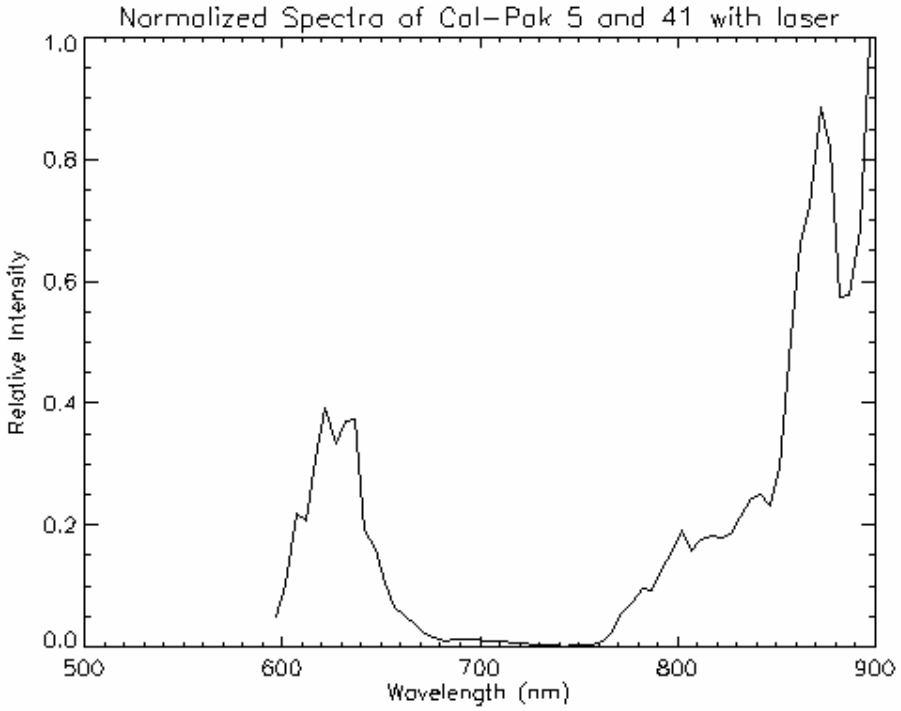

Figure 57: Normalized spectra of Cal-Pak 5 and 41 LEDs with laser reconstructed using 10 iterations of MART.

Natural vs. Manmade

The natural verses manmade test was performed to verify if the instrument was able to discern the spectral difference between natural and camouflaged manmade objects. Using the same data that was collected for the ranging test in figure 48-a, the spectra of the tank and personnel mines and vegetation (oleanders and olive) was reconstructed using 20 iterations of the MART algorithm. Reference spectra were obtained using the Ocean Optics spectrometer. The defining spectral feature that was observed with the reference spectrometer in both of the natural vegetation samples (Figure 58-c and 58-d) was a small absorption near 700nm. This feature was not present in both of the landmines reference spectra (Figure 58-a and 58-d), where the spectra are relatively flat near 700nm. The reconstructed and reference spectrums are shown below in the following figures. Please note that the horizontal and vertical scales are not the same between the test and reference data.

From the spectra in figure 58, the absorption feature at 700nm was not as prominent in the reconstructed spectra (Figure 58 right) as in the reference spectra (Figure 58 left). However, a strong absorption near 850nm was present in both of the reconstructed landmine spectra (Figure 58-a and 58-b) and not present in the reconstructed vegetation spectra (Figure 58-c and 58-d). Unfortunately due to the passband of the reference spectra, the absorption feature at 850nm could not be verified.

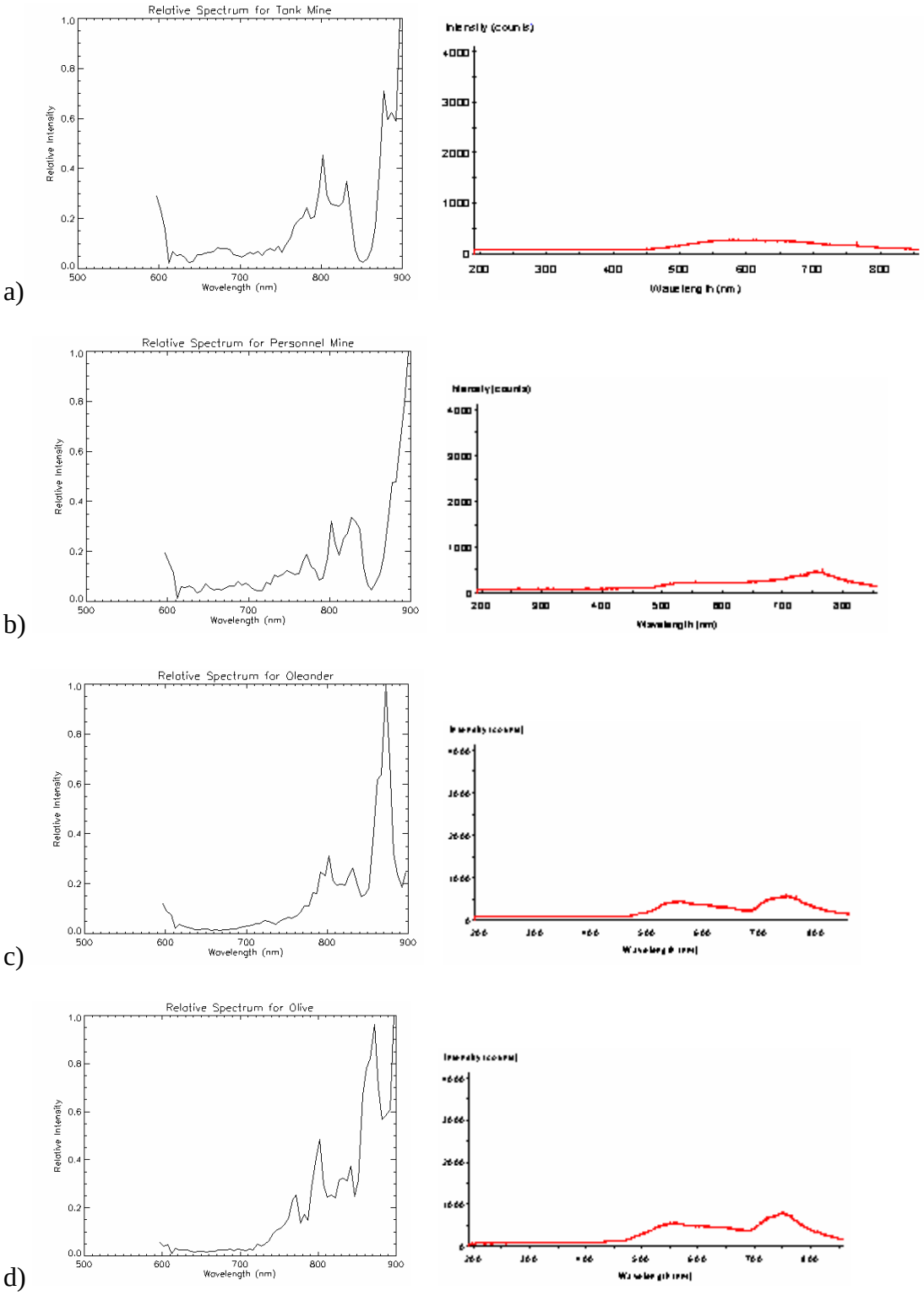

Figure 58: Reconstructed Spectra (left) and reference spectra (right) of the targets a) Large tank mine, b) Small personnel mine, c) Oleanders topside, and d) Olive.

Quantum Efficiency Removal:

In the previous sections for the spectral test section, the reconstructed spectra that were shown had large spikes on the long wavelength end that are not present in the reference data. It was believed that this artifact was a result of the resposivity of the image intensifier. To correct this problem, the responsivity of the image intensifier needs to be removed from the spectral intensity point spread functions before they are used to generate the spectral calibration matrix **H**. Unfortunately, the camera (including the intensifier) was returned to Sandia and the response of the image intensifier could not be measured directly. However, using a data sheet provided by the image intensifier manufacturer, a quantum efficiency plot was generated using a linear interpolation and is shown in Figure 59.

The generated quantum efficiency data was then used to scale the calibration matrix. To scale the calibration matrix **H**, the 61 images used for the 597nm – 897nm with $\Delta\lambda$ = 5nm spectral calibration were each divided by the quantum efficiency value at their respective wavelengths. The images were then used to generate a new calibration matrix **H** that now accounts for the efficiency of the image intensifier.

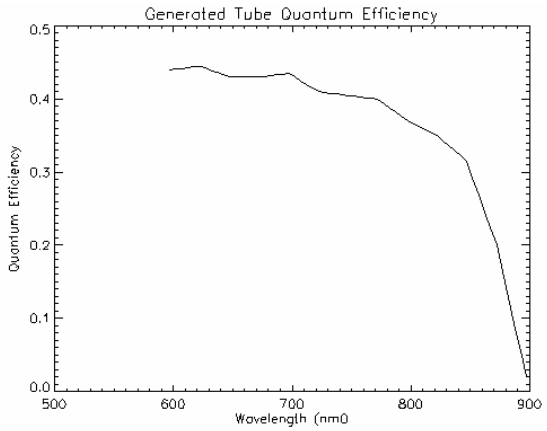

Figure 59: Generated quantum efficiency plot for the image intensifier.

With the new calibration matrix formed, data consisting of an image of the Cal-Pak 41 LED (λ_{peak} = 623.566nm) imbedded in a Styrofoam target was reconstructed using both the new quantum efficiency scaled and uncorrected matrices. These spectra are shown in Figure 60.

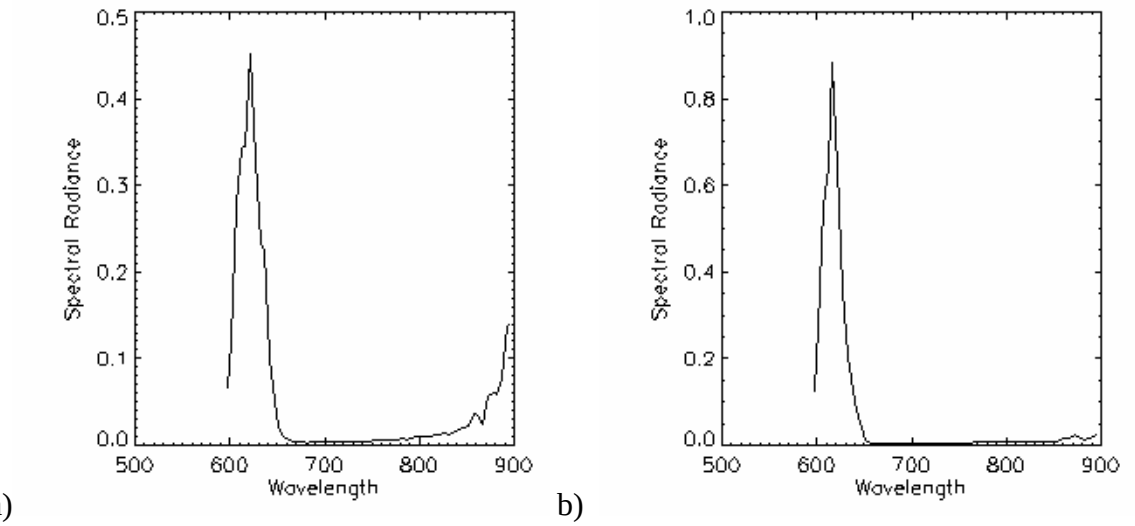

a) b)

Figure 60: Reconstructed spectra of the Cal-Pak 41 LED (λ_{peak} = 623.566nm) using 5 iterations of MART for the same pixel using the a) Uncorrected calibration matrix and b) Quantum efficiency scaled calibration matrix.

Notice that in figure 60-a, the reconstruction artifact is present in the long end of the spectra and in figure 60-b the artifact is greatly reduced (approximately by a factor of 5). This test was then repeated with the laser emitter illuminating the same target.

Figure 61 is the 0^{th} order image of the target where the bright spot in the figure is the illuminated LED. What can be qualitatively seen from this image is that the background of the target, illuminated only by the laser illumination, is dimmer than the portion of the target where the LED is located. Therefore, all reconstructed spectra of the pixels on the image that contain the LED would have two peaks. These two peaks would be a tall spike from the LED and a smaller spike for the laser emitter. The reconstructed spectra from a pixel on the LED portion of the image are shown in Figure 62. The spectra were reconstructed using both the quantum efficiency scaled and uncorrected matrices. Notice the relationship of the heights of the two peaks in the reconstructed spectra in Figure 62. The reconstructed spectra using the quantum efficiency scaled matrix has the LED peak larger than the laser emitter as expected from the image of the 0^{th} order in Figure 61. The reconstructed spectra using the uncorrected matrix have the laser return spike taller than the LED spike.

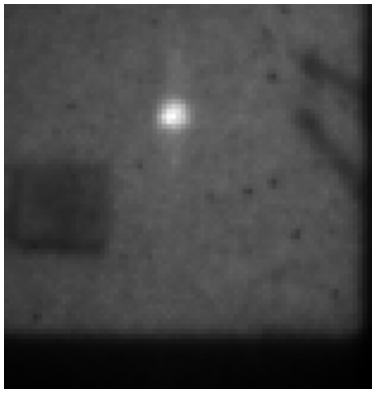

Figure 61: 0^{th} order image of the diffraction pattern for the LED (λ_{peak} = 623.566nm) test (LED is the bright spot)

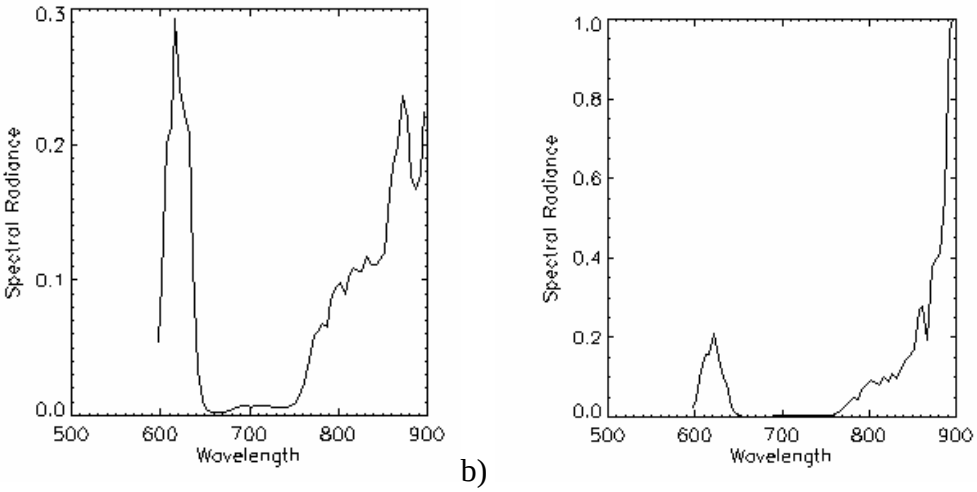

a) b)

Figure 62: Reconstructed spectra of an LED (λ_{peak} = 623.566nm) with the laser emitter on using 5 iterations of MART for the same pixel using the a) Quantum efficiency scaled calibration matrix and b) Uncorrected calibration matrix.

Conclusions:

An instrument called the Ranging-Imaging Spectrometer has been demonstrated by combining the Computed Tomographic Imaging Spectrometer (CTIS) and a Scannerless range Imaging LADAR (LADAR). The device is capable of simultaneously measuring hyperspectral data and 3-D spatial data is a sequence of 8 continuous image frames. There are no pixel registrations problems between the spectral and range data because the sub-systems are using the same focal plane array. The spectral data is acquired at each of the 8 images that are required to measure the range. The instrument

has 77 x 77 pixel spatial sampling covering a $\pm 6.25^{o}$ field of view, 17.56cm range resolution, and 61 spectral bands.

Range tests have shown that the CTIS lowers the lateral resolution of the range reconstruction by 67%. The loss of lateral resolution is attributed to optical aberrations in the CTIS and the low spatial sampling of the combined instrument. These tests have also shown that the RIS is capable of measuring range on smooth objects that are subtending a major portion of the field of view.

Spectral tests using LED sources have shown that the CTIS is able to resolve spectral lines that are separated by 19nm. The instrument is able to discriminate between natural "green" vegetation and camouflaged manmade objects by detecting an absorption feature near 850nm. Spectra tests have also shown that removing the response of the image intensifier greatly reduces artifacts incurred by the spectral reconstruction procedure at the long end of the passband of the RIS.

A range correction technique was developed to reduce the range reconstruction error caused by ambient light used for the spectral measurement by a factor of 10. This promising technique can be applied to other situations where the desired signal is buried in the noise.

Summary of the most important results

-The effect of ambient light on the range calculation

The original design for the SRI LADAR had a narrow band filter ($\Delta\lambda$ = 10nm) centered on the laser wavelength. The filter was responsible for eliminating ambient light. Since the CTIS uses the ambient light for spectral information, the filter had to be removed. The focal plane has a non-linear relationship between the mean and the variance of the pixel value distribution. The added signal due to the ambient light has raised the mean signal value to a level where this non-linear relationship is affecting the range reconstruction.

To correct for this error caused by the non-linear response of the focal plane, a technique using random variable distributions was developed and implemented. This technique, referred to as variance shaping, is based on the fact that the mean value of the pixel distributions is linear with signal. The variance shaping technique involves measuring the mean and variance of the pixel distribution values for the instrument by illuminating a target only with the laser light. The target is large enough to fill the entire field of the instrument. The mean and variance are calculated at a variety of distances between the sensor and target. The measured mean and variances are then used in a mean-variance look-up table for the correction technique.

In order to correct the range measurement, two sets of data are taken of the scene. One set of data has the laser and ambient light, and the second set contains only the ambient light. The two data sets are then subtracted yielding a set of data that contains only the laser light. The mean of this set is then calculated and then the mean-variance look-up table is consulted to determine the corresponding variance. This value is referred to as the “ideal variance”, because it is the variance that the pixel distribution would have if there was no ambient light.

Then going back to the data that contains the laser and ambient light, the pixel distribution is then shaped using random variable distributions to reduce the variance to the ideal variance value. This shaped data is then fed into the range algorithm and the range of the scene is determined. Laboratory results have shown this technique to reduce the average range error by a factor of 10 from 26cm to 2.6cm.

Listing of all publications and technical reports supported under this grant or contract. Provide the list with the following breakout, and in standard format showing authors, title, journal, issue, and date.

(a) Papers published in peer-reviewed journals

-N/A

(b) Papers published in non-peer-reviewed journals or in conference proceedings

[1] B. A. Kinder, J.P. Garcia, E.L. Dereniak "Development of a 4-Dimensional Imaging Spectrometer", Imaging Spectrometry VIII, Proceedings of SPIE Vol. 4816 pp. 381-388

[2] Brian A. Kinder, John P. Garcia, Robert D. Habbit, and Eustace L. Dereniak, "Ranging-Imaging Spectrometer", Imaging Spectrometry IX, Proceedings of SPIE Vol. 5159, pp.73-81

(c) Papers presented at meetings, but not published in conference proceedings

-N/A

(d) Manuscripts submitted, but not published

Brian A. Kinder and Eustace L. Dereniak, "Using Random Variable Distributions for Noise Reduction in Range Reconstructions", Optical Engineering, Submitted November 2004

(e) Technical reports submitted to ARO

[1] Brian A. Kinder and Eustace L. Dereniak, "Technical Report for the Spectral LADAR Receiver Project April-June"

[2] Brian A. Kinder and Eustace L. Dereniak, "Technical Report for the Spectral LADAR Receiver Project July-September 2003"

This List of all participating scientific personnel showing any advanced degrees earned by them while employed on the project.

Brian A. Kinder-Masters of Science in Optical Sciences, The University of Arizona, December 2002.

Brian A. Kinder-Doctor of Philosophy in Optical Sciences, The University of Arizona, May 2005-expected.

Report of Inventions (by title only)

Ranging-Imaging Spectrometer

Bibliography

[1] CTIS Optical Design Program written by Dr. Curtis Volin of the: Optical Detection Lab, University of Arizona, Optical Science Center, Tucson AZ, 85721

[2] Colin L. Smithpeter, Robert O. Nellums, Steve M. Lebien, George Studor, "A Miniature, High-Resolution Laser Radar Operating at Video Rates", Proc. SPIE Vol. 4035, P. 279-286, Laser Radar Technology and Applications V, Kamerman, Gary W.; Singh, Upendra N.; Werner, Christian H.; Molebny, Vasyl V.

[3] J.P. Garcia, E.L. Dereniak, P.T. Spuhler, *Four Dimensional Imager*, Optical Detection Lab, Optical Science Center, University of Arizona, Tucson, AZ, 85721, DARPA funding proposal.

[4] B. A. Kinder, J.P. Garcia, E.L. Dereniak "Development of a 4-Dimensional Imaging Spectrometer" Imaging Spectrometry VIII, Proceedings of SPIE Vol. 4816 pp. 381-388

[5] C. E. Volin Et al., *Demonstration of a MWIR High Speed Non-scanning Imaging Spectrometer*, Automatic Target Recognition IX, Proceedings of SPIE Vol. 3718 pp. 480-489

[6] Brian A. Kinder, John P. Garcia, Robert D. Habbit, and Eustace L. Dereniak, "Ranging-Imaging Spectrometer, Imaging Spectrometry IX, Proceedings of SPIE Vol. 5159, pp.73-81

[7] B. R. Frieden, "Probability, Statistical Optics, and Data Testing 2nd Ed.", Springer-Verlag 1991

[8] Curtis E. Volin, "Portable Snapshot Infrared Imaging Spectrometer", Ph.D. dissertation, The University of Arizona, 2000.

Appendixes

None